ARTICLE

https://doi.org/10.1038/s41586-019-1232-1

Metabolic control of BRISC–SHMT2 assembly regulates immune signalling

Miriam Walden[1,9], Lei Tian[2,9], Rebecca Ross[3], Upasana M. Sykora[1], Dominic P. Byrne[4], Emma L. Hesketh[1], Safi K. Masandi[1], Joel Cassel[5], Rachel George[1], James R. Ault[1], Farid El Oualid[6], Krzysztof Pawłowski[7,8], Joseph M. Salvino[5], Patrick A. Eyers[4], Neil A. Ranson[1], Francesco Del Galdo[3], Roger A. Greenberg[2]* & Elton Zeqiraj[1]*

Serine hydroxymethyltransferase 2 (SHMT2) regulates one-carbon transfer reactions that are essential for amino acid and nucleotide metabolism, and uses pyridoxal-5′-phosphate (PLP) as a cofactor. Apo SHMT2 exists as a dimer with unknown functions, whereas PLP binding stabilizes the active tetrameric state. SHMT2 also promotes inflammatory cytokine signalling by interacting with the deubiquitylating BRCC36 isopeptidase complex (BRISC), although it is unclear whether this function relates to metabolism. Here we present the cryo-electron microscopy structure of the human BRISC–SHMT2 complex at a resolution of 3.8 Å. BRISC is a U-shaped dimer of four subunits, and SHMT2 sterically blocks the BRCC36 active site and inhibits deubiquitylase activity. Only the inactive SHMT2 dimer—and not the active PLP-bound tetramer—binds and inhibits BRISC. Mutations in BRISC that disrupt SHMT2 binding impair type I interferon signalling in response to inflammatory stimuli. Intracellular levels of PLP regulated the interaction between BRISC and SHMT2, as well as inflammatory cytokine responses. These data reveal a mechanism in which metabolites regulate deubiquitylase activity and inflammatory signalling.

SHMT2 functions in one-carbon folate metabolism that supports the purine and thymine synthesis that is required for cell growth and proliferation. Full-length SHMT2 localizes to mitochondria through an N-terminal mitochondria-targeting sequence; an N-terminal truncation that removes residues 1–21 generates the cytoplasmic SHMT2α isoform[1,2] (Fig. 1a). PLP, the active form of vitamin B6, promotes a shift in the SHMT2 oligomeric state from an inactive dimer to the enzymatically active tetramer[1,3].

SHMT2 also controls inflammatory cytokine signalling through its interaction with the BRISC deubiquitylase (DUB). BRCC36 is a JAMM (JAB1, MOV34, and MPR1, PAD1 N-terminal (MPN) family) Zn^{2+}-dependent DUB and functions within two macromolecular complexes, which requires interaction with MPN^{-} pseudo-DUBs Abraxas 1 or Abraxas 2 for DUB activity[4–6] (Fig. 1a). The nuclear Abraxas 1 isopeptidase complex (ARISC) complex partners with RAP80 and BRCA1, and forms the BRCA1-A complex that is required for DNA repair[7–10]. Direct interaction with SHMT2 enhances the delivery of BRISC to ubiquitylated type I interferon (IFN) receptors (IFNAR1 and IFNAR2)[11,12], which allows BRCC36 to deubiquitylate the lysine-63-linked ubiquitin chains (Ub(K63)) on IFNAR1 and IFNAR2 and limits the endocytosis and lysosomal degradation of these receptors[12]. BRISC-deficient mice exhibit attenuated IFN responses and are protected from pathological conditions that stem from increased levels of inflammatory signalling[12]. The association between BRISC and SHMT2 therefore provides a potential link between metabolism and inflammation.

The BRCC36–Abraxas 2 complex is an obligate dimer of heterodimers that is essential for DUB activity and IFN signalling[13,14]. Similarly, BRISC and ARISC are active as stable dimers of tetramers with stoichiometry 2:2:2:2 (refs. [4,5,13,15]). Structures of the human BRISC are currently unavailable, and the molecular basis for SHMT2 binding and regulation is unknown. We present the cryo-electron microscopy (cryo-EM) structure of the BRISC–SHMT2 complex at a resolution of 3.8 Å, which reveals the BRISC architecture and the molecular basis of the inhibition of DUB activity by SHMT2. Structure-guided mutations or increasing intracellular levels of PLP reduced the interaction between BRISC and SHMT2 as well as inflammatory signalling, which reveals a direct link between vitamin B6 metabolism and control of immune responses.

SHMT2 is an endogenous BRISC inhibitor

We produced SHMT2ΔN (residues 18–504), which lacks the mitochondria-targeting sequence and is a mixture of dimers and tetramers in solution (Fig. 1b). Tetramer peak fractions absorbed strongly at 435 nm, which indicates association with PLP and is consistent with previous findings that PLP binding promotes a shift from an inactive dimer to the active SHMT2 tetramer[1] (Fig. 1c, Extended Data Fig. 1a, b). Dimer and tetramer peaks were confirmed by native mass spectrometry (Extended Data Fig. 1c).

A serendipitous SHMT2(A285T) substitution near the PLP-acceptor residue (K280) was identified by the Structural Genomics Consortium (RCSB Protein Data Bank (PDB) code 6DK3). SHMT2ΔN(A285T) is dimeric in solution and crystal lattice, which enables a direct comparison between dimer (apo enzyme) and tetramer (holoenzyme) structures (Extended Data Fig. 1a–d). Structures of individual wild-type SHMT2α and SHMT2ΔN(A285T) protomers are similar, which suggests that the A285T substitution does not substantially perturb the structure (Extended Data Fig. 1e). However, the A285T substitution reduces covalent PLP association, subsequent tetramerization and catalytic activity (Extended Data Fig. 2a, b). The addition of PLP induced a transition from the dimer to the tetramer form of SHMT2ΔN, which led to a large shift in thermal melting temperature (Extended Data Fig. 2c, d). This shift was largely reduced or abolished

[1]Astbury Centre for Structural Molecular Biology, School of Molecular and Cellular Biology, Faculty of Biological Sciences, University of Leeds, Leeds, UK. [2]Department of Cancer Biology, Basser Center for BRCA, Perelman School of Medicine, University of Pennsylvania, Philadelphia, PA, USA. [3]Leeds Institute of Rheumatic and Musculoskeletal Medicine, University of Leeds, Leeds, UK. [4]Department of Biochemistry, Institute of Integrative Biology, University of Liverpool, Liverpool, UK. [5]The Wistar Cancer Center for Molecular Screening, The Wistar Institute, Philadelphia, PA, USA. [6]UbiQ Bio BV, Amsterdam, The Netherlands. [7]Warsaw University of Life Sciences, Warsaw, Poland. [8]Department of Translational Medicine, Clinical Sciences, Lund University, Lund, Sweden. [9]These authors contributed equally: Miriam Walden, Lei Tian. *e-mail: rogergr@pennmedicine.upenn.edu; e.zeqiraj@leeds.ac.uk

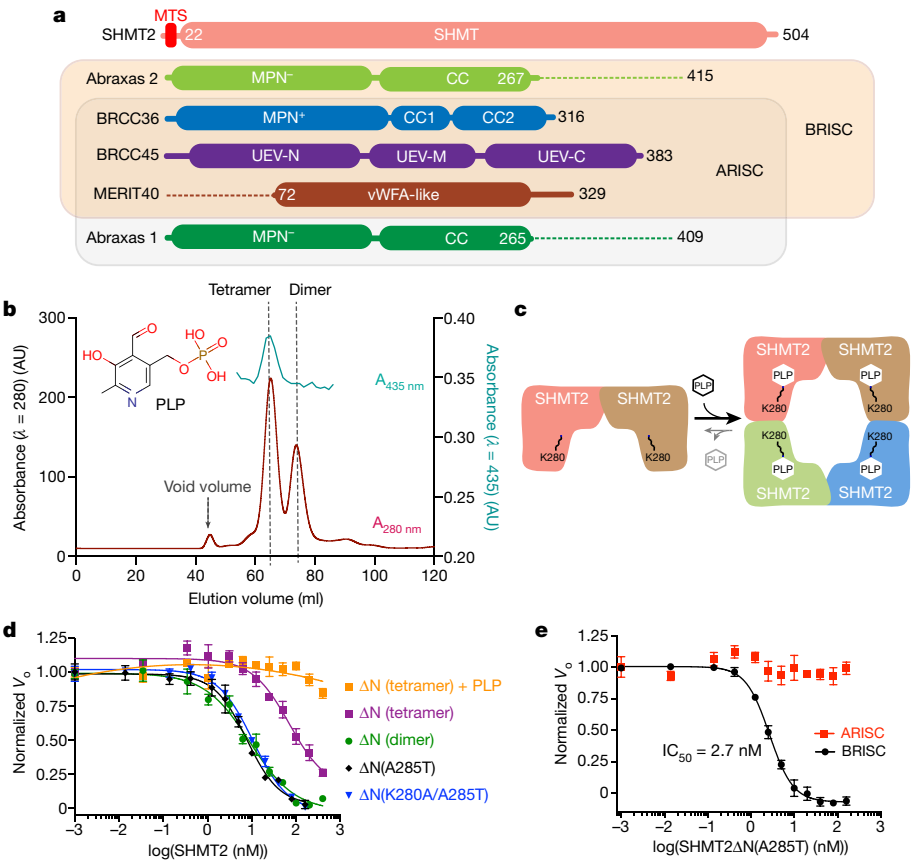

Fig. 1 | SHMT2 dimer inhibits BRISC DUB activity. a, Domain architecture of SHMT2 and BRCC36-containing complexes. MTS, mitochondria-targeting sequence; CC, coiled coil. **b**, SHMT2ΔN elution profile after size-exclusion chromatography, monitored by measuring absorbance at 280 nm. SHMT2ΔN bound to PLP was detected by measuring absorbance at 435 nm. Data are representative of three independent experiments. AU, arbitrary units. **c**, Schematic of SHMT2ΔN dimer–tetramer equilibrium in response to PLP binding. **d**, BRISC DUB activity against a fluorogenic K63-linked diUb substrate in the presence of various forms of SHMT2ΔN. **e**, BRISC and ARISC DUB activity against a fluorogenic K63-linked diUb substrate in the presence of SHMT2ΔN(A285T). Data in **d**, **e** are mean ± s.e.m. of three independent experiments carried out in duplicate.

in SHMT2(A285T) and SHMT2(K280A) mutants, which is consistent with studies that show that alterations of SHMT2 that abrogate PLP binding shift the equilibrium towards the dimer[1,16–19] (Extended Data Fig. 2e).

The addition of SHMT2ΔN inhibited the DUB activity of BRISC (Fig. 1d). Dimeric SHMT2ΔN was a better inhibitor (half maximal inhibitory concentration (IC_{50}) = 9 nM) than the tetrameric form (IC_{50} = 77.5 nM). Because the SHMT2ΔN tetramer is not fully saturated with PLP (Extended Data Fig. 2c, d), preincubation with PLP further reduced BRISC inhibition by the SHMT2ΔN tetramer (Fig. 1d). The obligate dimers SHMT2ΔN(A285T) and SHMT2ΔN(K280A/A285T) were effective inhibitors of BRISC and similar to SHMT2ΔN dimers (Fig. 1d). SHMT2ΔN(A285T) DUB inhibition was selective for BRISC as compared to ARISC (Fig. 1e), which confirms that SHMT2 does not interact with the ARISC[12]. These data suggest a previously unknown role for the dimeric (PLP-free) form of SHMT2 in regulating the DUB activity of BRISC.

Structure of the BRISC–SHMT2 complex

To understand the molecular basis of the BRISC–SHMT2 association, and how PLP-dependent SHMT2 oligomerization affects DUB activity, we solved the structure of the BRISC bound to an SHMT2 dimer. Using limited proteolysis, we identified a minimal complex—which we term BRISCΔNΔC (Extended Data Fig. 3a, b)—that contains BRCC36, BRCC45, MERIT40ΔN (residues 72–329) and Abraxas 2ΔC (residues 1–267). BRISC and BRISCΔNΔC were active towards a fluorogenic K63-linked diubiquitin (diUb) substrate (Extended Data Fig. 3c) and both were inhibited by SHMT2ΔN(A285T), with similar IC_{50} values (Extended Data Fig. 3d). SHMT2ΔN(A285T) formed a stable equimolar complex with BRISCΔNΔC (Extended Data Fig. 3e, f).

We used negative-stain electron microscopy and single-particle cryo-EM to evaluate BRISCΔNΔC and the BRISCΔNΔC–SHMT2ΔN(A285T) complex. BRISCΔNΔC particles showed distinct U-shaped assemblies that were similar to those seen for the nuclear ARISC[15]. However, BRISCΔNΔC showed heterogeneity and flexibility of the 'arm' regions (Extended Data Fig. 4a). The BRISCΔNΔC–SHMT2ΔN(A285T) complex was homogeneous, with SHMT2ΔN(A285T) bridging both arms of the U-shaped BRISC structure in two-dimensional class averages (Extended Data Fig. 4a). We collected a large cryo-EM dataset and identified 71,262 particles (approximately 11%) with a structure with apparent C2 symmetry that contained a central trapezoidal region and two extending arms. The remaining particles form a structure that is missing one arm (Extended Data Fig. 4b, c). After three-dimensional classification and refinement, using both C1 and C2 symmetry, we obtained electron microscopy density maps at resolutions of 3.8 Å and 4.2 Å, respectively (Extended Data Fig. 4c, d, Extended Data Table 1).

The BRISCΔNΔC comprises a central core region and two extending arms. We fit the structure of insect BRCC36–Abraxas 2 (PDB code 5CW3)[13] at the base of the map; the quality of the electron microscopy density in this region was sufficient for modelling the human BRCC36–Abraxas 2 sequence into the structure (Fig. 2). The SHMT2ΔN(A285T) dimer was immediately recognizable in the electron microscopy map, with the structure (PDB code 6DK3) fitting directly above the MPN domains of BRCC36–Abraxas 2 (Fig. 2). The remaining unoccupied

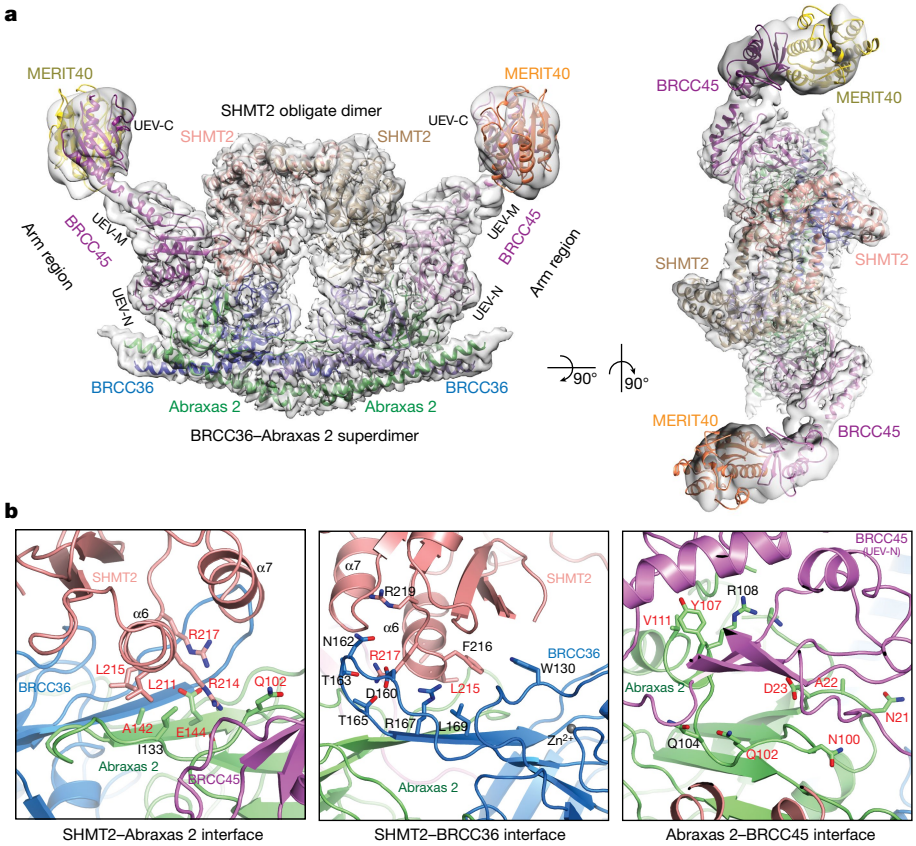

Fig. 2 | Structure of the BRISC–SHMT2 complex. a, Cryo-EM density at contour level of 0.055 (C2 map), shown in transparent surface. Proteins are depicted as cartoon models. Owing to low resolution in the extended arm regions, UEV-C (BRCC45) and vWFA (MERIT40) models are shown for size comparison only. **b**, Close-up view of BRISC–SHMT2 interfaces. Residues labelled in red were altered in validation analysis.

density belongs to BRCC45 and MERIT40, for which no experimental structures are available.

BRCC45 contains two ubiquitin E2 variant (UEV) domains at its N and C termini. We used the FFAS03[20] and HHpred[21] algorithms to search for additional domains and identified a putative 'UBC-like' domain within residues 144–280, which suggests the presence of a middle UEV domain (UEV-M). Tandemly repeated domains are common during protein evolution, which provides reinforcement for the independent prediction of a third UEV domain in BRCC45 (ref. [22]) (Fig. 1a). Consistent with this hypothesis, we manually built a Cα-backbone structure for two consecutive UEV domains of BRCC45 into the density that immediately extends from Abraxas 2 (Fig. 2a). However, owing to the low resolution of this region, precise assignment of the sequence was not possible.

We used the structure of the related ARISC[15] as a guide to place homology models of MERIT40 and a third UEV (BRCC45) domain within the 'fist-like' density in the distal region of each arm (Fig. 2a). The resolution in this peripheral region is poor (approximately 10 Å), and it was therefore not possible to ascertain the precise orientation of the von Willebrand factor type A (vWFA) and UEV-C domains of MERIT40 and BRCC45, respectively. We modelled UEV-N and UEV-C in proximity to Abraxas 2 and MERIT40, respectively, in accordance with previous deletion studies[4,23] (Fig. 2a). Thus, we built a complete BRISC–SHMT2 model using a combination of known structures, de novo model building and homology modelling (Fig. 2a). The 'core' structure—consisting of the BRCC36–Abraxas 2 superdimer and the SHMT2 obligate dimer—is well-resolved, with a local resolution of 3.5–4.0 Å (Extended Data Figs. 4c, d, 5a, b).

SHMT2 bridges the two arms of the BRISC and sits directly above the BRCC36–Abraxas 2 superdimer, which explains the requirement for superdimer formation in SHMT2 binding[13]. SHMT2 interacts with MPN domains of BRCC36 and Abraxas 2, and UEV-N and UEV-M domains of BRCC45 (Fig. 2a). The main BRISC-interacting surface on SHMT2 is centred on the two α6 helices; proximal residues between SHMT2–Abraxas 2, SHMT2–BRCC36 and Abraxas 2–BRCC45 are shown in Fig. 2b. MERIT40 does not contact SHMT2 directly (Fig. 2a), and its position may provide stabilizing interactions with BRCC45 while also interacting with other signalling molecules[24]. A comparison between human and insect BRCC36–Abraxas 2 superdimers reveals a similar overall structure, with minor local shifts (Extended Data Fig. 5c–e). Overall, the structure provides a view of the interaction surfaces between SHMT2 and components of the BRISC.

Previous work suggested that the BRISC also interacts with SHMT1 in cells, although cellular BRISC–SHMT2 complexes were much more abundant[12]. To test whether SHMT2 and SHMT1 interact equally with BRISC in vitro, we purified SHMT1 dimers and tetramers; we failed to assemble BRISC–SHMT1 complexes and observed no inhibition of BRISC DUB activity in vitro (Extended Data Fig. 6). Although it remains possible that BRISC–SHMT1 complexes form in cells, we predict these will be of lower affinity in comparison with BRISC–SHMT2 complexes, and may be a consequence of indirect interactions with other factors.

We altered SHMT2 residues in proximity to BRISC (Fig. 2b), and assessed their effects on DUB activity in vitro. Residue substitutions were made in the SHMT2ΔN(A285T) background, which purifies as a dimer (Extended Data Fig. 7a, b). SHMT2ΔN(A285T) variants containing L211R or L215R were each less-potent inhibitors of BRISC DUB activity as compared to SHMT2ΔN(A285T), and the SHMT2ΔN(A285T/L211R/L215R) mutant had no detectable inhibitory effect on BRISC activity (Extended Data Fig. 7c). SHMT2ΔN inhibition was also observed with hexa-ubiquitin (hexaUb) chains as substrates (Extended Data Fig. 7d). DUB activity was only marginally reduced when assayed with SHMT2ΔN(A285T/L211R/L215R), SHMT2ΔN tetramers or SHMT1, which mirrors results obtained with

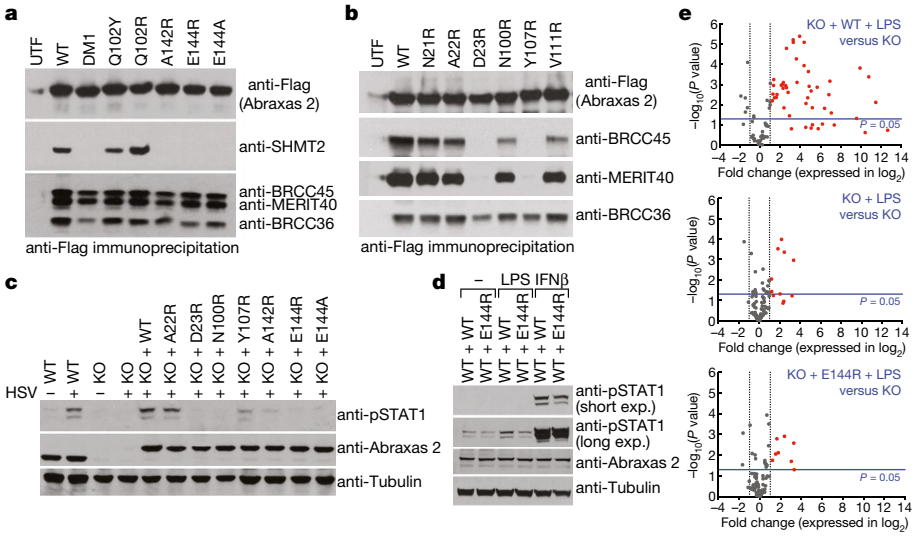

Fig. 3 | BRISC–SHMT2 interaction is important for interferon signalling. a, **b**, Immunoprecipitation was performed using anti-Flag antibody in HEK293T cells transiently transfected with Flag–haemagglutinin (HA) epitope-tagged Abraxas 2 wild type (WT) or mutants. Immunoblotting was performed for the indicated proteins. UTF, untransfected cells. **c**, *Abraxas2*$^{-/-}$ (KO) MEFs and *Abraxas2*$^{-/-}$ MEFs stably reconstituted with wild-type or mutant Abraxas 2 were infected with HSV that lacks the lytic phase gene *ICP0*. IFN signalling was assessed by immunoblotting for STAT1 phosphorylated at Y701 (pSTAT1). **d**, Wild-type MEFs that overexpress wild-type Abraxas 2 (WT +WT) or Abraxas 2(E144R) (WT +E144R) were challenged with LPS and IFNβ. IFN signalling was assessed as in **c**. Data in **a**–**d** are representative of three independent experiments. For gel source data, see Supplementary Fig. 1. **e**, Volcano plots illustrating the fold change in gene expression of IFN-type I-stimulated genes relative to *Abraxas2*$^{-/-}$ MEFs without LPS treatment. *P* values were calculated using a Student's *t*-test (two-tailed distribution and equal variances between the two samples) on the triplicate $2^{-\Delta Ct}$ values for each gene in each treatment group compared to the control group. Genes below the $P = 0.05$ threshold were upregulated in wild type with LPS, but represented as below statistical significance owing to the relative expression in *Abraxas2*$^{-/-}$samples being almost zero. Regulated genes are highlighted in Extended Data Fig. 9a.

fluorescently labelled diUb and is consistent with the observation that the L211R/L215R double substitution reduces BRISC–SHMT2 interaction in vitro (Extended Data Fig. 8a). These experiments establish the SHMT2 α6 helix as the most important contact surface for BRISC interaction and inhibition of DUB activity.

BRISC–SHMT2 affects immune signalling

To understand the relevance of the BRISC–SHMT2 interaction in cells, we altered interface residues between SHMT2, Abraxas 2 and BRCC45 (Fig. 2b) and assessed interactions by co-immunoprecipitation (Fig. 3a, b). Consistent with the loss of interaction with SHMT2, the Abraxas 2 mutants A142R, E144A and E144R expressed in *Abraxas2*$^{-/-}$ mouse embryonic fibroblasts (MEFs) showed reduced STAT1 phosphorylation in response to infection with herpes simplex virus (HSV); this was also true for N100R, Y107R and D23R mutants, which either reduce or prevent BRCC45–MERIT40 binding (Fig. 3c). The BRISC–SHMT2 interaction was also required for immune signalling when cells were challenged using lipopolysaccharide (LPS) or IFNβ (Fig. 3d). Moreover, we observed increased IFNAR1 ubiquitylation after IFN stimulation in cells that overexpressed the Abraxas 2 E144R mutant (Extended Data Fig. 7e).

For a broader view of immune signalling output that is dependent on the BRISC–SHMT2 complex, we performed quantitative PCR with reverse transcription (qRT–PCR) analysis of 79 genes that are often upregulated during a type I interferon response. Ectopic expression of wild-type Abraxas 2 resulted in 48 genes being upregulated between 2- and 8,000-fold in response to LPS (Fig. 3e, Extended Data Fig. 9a). Accordingly, LPS challenge of *Abraxas2*$^{-/-}$ cells or *Abraxas2*$^{-/-}$ cells ectopically expressing Abraxas 2(E144R) showed a poor response, with 11 and 8 genes, respectively, being upregulated between two- and tenfold compared to non-challenged *Abraxas2*$^{-/-}$ cells (Fig. 3e).

We next altered SHMT2 residues to ascertain their importance in cellular assembly of BRISC–SHMT2 complexes. Overexpression of SHMT2ΔN(L211R/L215R) resulted in the loss of BRISC–SHMT2 interaction in MEFs, which mirrors the results seen in vitro (Extended Data Figs. 7f, 8a). Levels of STAT1 phosphorylation were also affected in cells that were challenged with LPS (Extended Data Fig. 7g), and we observed increased IFNAR1 ubiquitylation after IFN stimulation of cells that overexpress the SHMT2ΔN(L211R/L215R) mutant (Extended Data Fig. 7e). Collectively, these findings reveal the specific Abraxas 2 and SHMT2 surfaces that are required for BRISC–SHMT2 complex assembly and immune signalling in cells.

The positioning of SHMT2 within the structure provides a potential rationale for its inhibition of DUB activity, as it blocks the BRCC36 active site (Extended Data Fig. 8b). Kinetic data suggest SHMT2 acts as an apparent competitive inhibitor (Extended Data Fig. 8c). However, the increase in K_m was only moderate (about twofold at equimolar BRISC-SHMT2 complex), which suggests that Ub(K63) chains might displace bound SHMT2 from BRISC when poly-ubiquitylated substrates are in close proximity. This model would account for the counterintuitive function of SHMT2 as both an inhibitor of BRISC activity and an essential mediator of BRISC association with sites of DUB action (Extended Data Fig. 10). It is also possible that other factors and post-translational modifications trigger SHMT2 dissociation from BRISC in cells. We propose that SHMT2 acts as a reversible endogenous BRISC inhibitor that prevents non-specific DUB activity. This regulated safety mechanism is similar in concept to protease inhibition by endogenous inhibitors[25]. To our knowledge, SHMT2 is the first example of an endogenous DUB inhibitor, which acts as a precedent for the possible regulation of other DUBs in vivo.

Regulation of BRISC–SHMT2 interaction by PLP

BRISC DUB inhibition provides the first non-enzymatic role of the SHMT2 dimer. Our structure explains why the apo SHMT2 dimer—but not the PLP-bound tetramer—inhibits DUB activity. The SHMT2 α6 helix interacts with BRISC, and this interaction interface overlaps with the SHMT2 tetramerization surface; this accounts for the observation that the SHMT2 tetramer and the BRISC–SHMT2 complexes are mutually exclusive (Extended Data Figs. 1b, 8d). The SHMT2ΔN–PLP tetramer does not form BRISC–SHMT2 complexes in vitro (Extended Data Fig. 8e), which suggests that PLP-induced tetramerization could

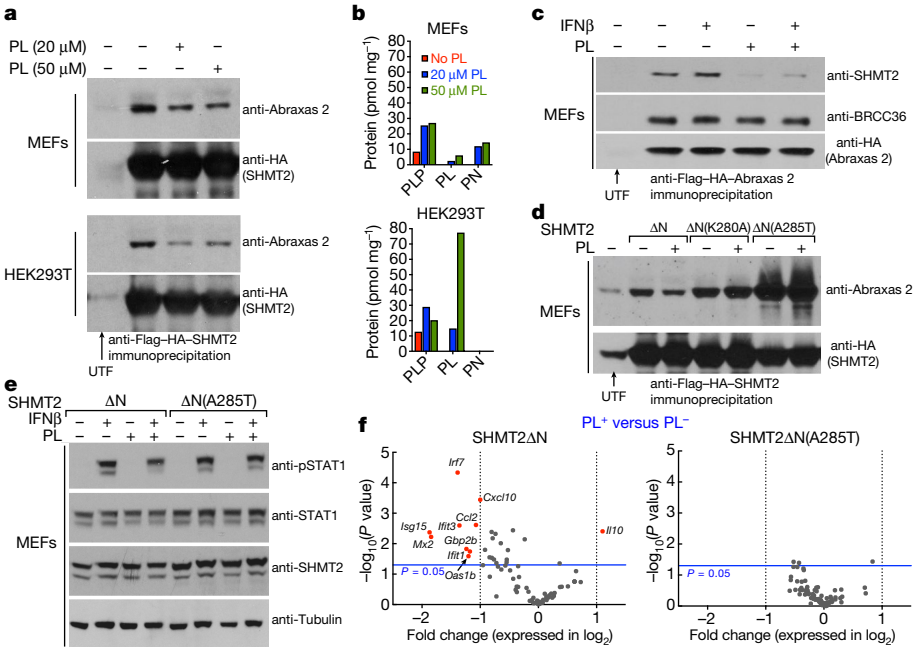

Fig. 4 | PLP regulation of BRISC-SHMT2 interaction and signalling. **a**, Immunoprecipitation of stably expressed Flag–HA epitope-tagged SHMT2ΔN using an anti-Flag antibody. Immunoblotting was performed after pyridoxal (PL) treatment for 48 h. **b**, Gas chromatography–mass spectrometry measurements of B6 vitamers from whole-cell lysates after culturing for 48 h in B6-vitamer-free medium, with and without pyridoxal. PN, pyridoxine. **c**, Immunoprecipitation of ectopically expressed Abraxas 2 using an anti-Flag antibody in MEFs grown in B6-vitamer-free medium for 48 h. Immunoblotting was performed for the indicated proteins after addition of 20 μM pyridoxal and/or 500 units per millilitre of mouse IFNβ. **d**, Immunoprecipitation using an anti-Flag antibody in MEFs stably expressing various Flag–HA epitope-tagged forms of SHMT2. Immunoblotting was performed after treatment with 20 μM pyridoxal for 48 h. **e**, Phosphorylated STAT1 levels in MEFs stably expressing various forms of SHMT2, and cultured in B6-vitamer-free medium. Cells were treated with 20 μM pyridoxal and/or 500 units per millilitre of IFNβ for 48 h. Data in **a**, **c**–**e** are representative of three independent experiments. For gel source data, see Supplementary Fig. 1. **f**, Volcano plots comparing type-1-IFN-induced gene expression in MEFs stimulated with LPS and cultured in the absence (PL^-) or presence (PL^+) of 20 μM pyridoxal. *P* values were calculated using a Student's *t*-test (two-tailed distribution and equal variances between the two samples) on the triplicate $2^{-\Delta Ct}$ values for each gene in each treatment group compared to the control group.

regulate SHMT2 dimer availability and BRISC–SHMT2 complex formation in cells.

To test this hypothesis, we cultured MEFs and HEK293T cells in B6-vitamer-free medium, and compared the BRISC–SHMT2 interaction after pyridoxal supplementation (Fig. 4a). PLP levels were confirmed by vitamin B6 metabolite measurements in whole-cell lysates (Fig. 4b), and fewer SHMT2 dimers were present after pyridoxal supplementation (Extended Data Fig. 9b). This coincided with a marked reduction of overexpressed SHMT2ΔN and endogenous Abraxas 2 interaction (Fig. 4a). Similarly, the interaction between overexpressed Abraxas 2 and endogenous SHMT2 was reduced (Fig. 4c). The PLP-dependent reduction of BRISC–SHMT2 interaction was not observed when PLP-resistant SHMT2 mutants were expressed (Fig. 4d).

We next measured levels of STAT1 phosphorylation, and observed a pyridoxal-dependent reduction of phosphorylated STAT1 upon IFNβ stimulation (Fig. 4e, Extended Data Fig. 9c). This reduction was not observed when PLP-resistant SHMT2 mutants were expressed (Fig. 4e, Extended Data Fig. 9d). Consistently, we observed an increase in both BRISC–SHMT2 complexes (Fig. 4d, Extended Data Fig. 9e) and levels of STAT1 phosphorylation when PLP-resistant SHMT2 mutants were expressed in cells cultured in B6-vitamer-containing medium and challenged with IFNβ or HSV (Fig. 4e, Extended Data Fig. 9d, f). Finally, we observed a pyridoxal-dependent reduction of nine IFN-induced genes in LPS-challenged MEFs that stably express SHMT2ΔN, but saw no change in MEFs in which a PLP-resistant mutant was expressed (Fig. 4f). IL10 was upregulated by 2.1-fold in pyridoxal-supplemented SHMT2ΔN cells (Fig. 4f) but not in LPS-stimulated MEFs containing wild-type Abraxas 2, which suggests that IL10 is not directly dependent on BRISC–SHMT2 (Extended Data Fig 9a). These experiments provide further evidence that PLP binding to SHMT2 regulates the BRISC–SHMT2 interaction and immune signalling in cells.

Endogenous small-molecule ligands that control ubiquitin signalling could be physiologically important. The influence of PLP on BRISC activity establishes a regulatory precedent for DUBs, akin to the plant hormone auxin and the second messenger inositol hexakisphosphate, which together allosterically regulate the activity of E3 ubiquitin ligases[26]. Post-translational modifications of the PLP acceptor-lysine[27,28] could provide additional layers of regulation of BRISC–SHMT2 association and immune signalling. It is possible that natural and synthetic SHMT2 binders—such as folate and PLP analogues—can modulate dimeric SHMT2 availability or conformation, and thus interferon signalling (Extended Data Fig. 10). Understanding the regulatory mechanisms of BRISC–SHMT2 interactions may therefore be useful for unlocking the potential of small-molecule ligands as therapeutic agents.

Online content

Any methods, additional references, Nature Research reporting summaries, source data, statements of data availability and associated accession codes are available at https://doi.org/10.1038/s41586-019-1232-1.

Received: 3 July 2018; Accepted: 29 April 2019;

1. Giardina, G. et al. How pyridoxal 5′-phosphate differentially regulates human cytosolic and mitochondrial serine hydroxymethyltransferase oligomeric state. *FEBS J.* **282**, 1225–1241 (2015).
2. Anderson, D. D., Woeller, C. F., Chiang, E.-P., Shane, B. & Stover, P. J. Serine hydroxymethyltransferase anchors de novo thymidylate synthesis pathway to nuclear lamina for DNA synthesis. *J. Biol. Chem.* **287**, 7051–7062 (2012).
3. Szebenyi, D. M., Liu, X., Kriksunov, I. A., Stover, P. J. & Thiel, D. J. Structure of a murine cytoplasmic serine hydroxymethyltransferase quinonoid ternary complex: evidence for asymmetric obligate dimers. *Biochemistry* **39**, 13313–13323 (2000).

4. Patterson-Fortin, J., Shao, G., Bretscher, H., Messick, T. E. & Greenberg, R. A. Differential regulation of JAMM domain deubiquitinating enzyme activity within the RAP80 complex. *J. Biol. Chem.* **285**, 30971–30981 (2010).
5. Cooper, E. M., Boeke, J. D. & Cohen, R. E. Specificity of the BRISC deubiquitinating enzyme is not due to selective binding to Lys63-linked polyubiquitin. *J. Biol. Chem.* **285**, 10344–10352 (2010).
6. Feng, L., Wang, J. & Chen, J. The Lys63-specific deubiquitinating enzyme BRCC36 is regulated by two scaffold proteins localizing in different subcellular compartments. *J. Biol. Chem.* **285**, 30982–30988 (2010).
7. Sobhian, B. et al. RAP80 targets BRCA1 to specific ubiquitin structures at DNA damage sites. *Science* **316**, 1198–1202 (2007).
8. Wang, B. et al. Abraxas and RAP80 form a BRCA1 protein complex required for the DNA damage response. *Science* **316**, 1194–1198 (2007).
9. Kim, H., Chen, J. & Yu, X. Ubiquitin-binding protein RAP80 mediates BRCA1-dependent DNA damage response. *Science* **316**, 1202–1205 (2007).
10. Jiang, Q. et al. MERIT40 cooperates with BRCA2 to resolve DNA interstrand cross-links. *Genes Dev.* **29**, 1955–1968 (2015).
11. Sowa, M. E., Bennett, E. J., Gygi, S. P. & Harper, J. W. Defining the human deubiquitinating enzyme interaction landscape. *Cell* **138**, 389–403 (2009).
12. Zheng, H. et al. A BRISC-SHMT complex deubiquitinates IFNAR1 and regulates interferon responses. *Cell Reports* **5**, 180–193 (2013).
13. Zeqiraj, E. et al. Higher-order assembly of BRCC36–KIAA0157 is required for DUB activity and biological function. *Mol. Cell* **59**, 970–983 (2015).
14. Walden, M., Masandi, S. K., Pawłowski, K. & Zeqiraj, E. Pseudo-DUBs as allosteric activators and molecular scaffolds of protein complexes. *Biochem. Soc. Trans.* **46**, 453–466 (2018).
15. Kyrieleis, O. J. P. et al. Three-dimensional architecture of the human BRCA1-A histone deubiquitinase core complex. *Cell Reports* **17**, 3099–3106 (2016).
16. Zanetti, K. A. & Stover, P. J. Pyridoxal phosphate inhibits dynamic subunit interchange among serine hydroxymethyltransferase tetramers. *J. Biol. Chem.* **278**, 10142–10149 (2003).
17. Jagath, J. R., Sharma, B., Rao, N. A. & Savithri, H. S. The role of His-134, -147, and -150 residues in subunit assembly, cofactor binding, and catalysis of sheep liver cytosolic serine hydroxymethyltransferase. *J. Biol. Chem.* **272**, 24355–24362 (1997).
18. Jala, V. R., Appaji Rao, N. & Savithri, H. S. Identification of amino acid residues, essential for maintaining the tetrameric structure of sheep liver cytosolic serine hydroxymethyltransferase, by targeted mutagenesis. *Biochem. J.* **369**, 469–476 (2003).
19. Krishna Rao, J. V., Jagath, J. R., Sharma, B., Appaji Rao, N. & Savithri, H. S. Asp-89: a critical residue in maintaining the oligomeric structure of sheep liver cytosolic serine hydroxymethyltransferase. *Biochem. J.* **343**, 257–263 (1999).
20. Xu, D., Jaroszewski, L., Li, Z. & Godzik, A. FFAS-3D: improving fold recognition by including optimized structural features and template re-ranking. *Bioinformatics* **30**, 660–667 (2014).
21. Zimmermann, L. et al. A completely reimplemented MPI bioinformatics toolkit with a new HHpred server at its core. *J. Mol. Biol.* **430**, 2237–2243 (2018).
22. Björklund, A. K., Ekman, D. & Elofsson, A. Expansion of protein domain repeats. *PLOS Comput. Biol.* **2**, e114 (2006).
23. Hu, X. et al. NBA1/MERIT40 and BRE interaction is required for the integrity of two distinct deubiquitinating enzyme BRCC36-containing complexes. *J. Biol. Chem.* **286**, 11734–11745 (2011).
24. Guettler, S. et al. Structural basis and sequence rules for substrate recognition by tankyrase explain the basis for cherubism disease. *Cell* **147**, 1340–1354 (2011).
25. Hamilton, G., Colbert, J. D., Schuettelkopf, A. W. & Watts, C. Cystatin F is a cathepsin C-directed protease inhibitor regulated by proteolysis. *EMBO J.* **27**, 499–508 (2008).
26. Zheng, N. & Shabek, N. Ubiquitin ligases: structure, function, and regulation. *Annu. Rev. Biochem.* **86**, 129–157 (2017).
27. Yang, X. et al. SHMT2 desuccinylation by SIRT5 drives cancer cell proliferation. *Cancer Res.* **78**, 372–386 (2018).
28. Cao, J. et al. HDAC11 regulates type I interferon signaling through defatty-acylation of SHMT2. *Proc. Natl Acad. Sci. USA* **116**, 5487–5492 (2019).

Acknowledgements We thank F. Sicheri, J. Fontana, A. Berry, C. Simon, I. Nissim, F. Sobott, J. Cockburn and A. Moloney for useful discussions, and R. Thompson, A. Gordon, M. Iadanza and M. Fuller for technical support. This work was supported by a Sir Henry Dale Fellowship (Wellcome Trust and the Royal Society; 200523/Z/16/Z) to E.Z., MRC MC_PC-16050 grant to E.Z. and F.D.G., NIH R01 CA138835 and a Lupus Research Alliance Target Identification in Lupus grant to R.A.G and J.M.S., a BBSRC (BB/L021250/1) grant to N.A.R, a BBSRC TDRF grant BB/N021703/1 and North West Cancer Research grants CR1088, CR1097 to P.A.E., and a Polish National Science Centre grant (2014/15/B/NZ1/03359) to K.P. The University of Leeds mass spectrometry facility is supported by BBSRC (BB/E012558/1) and Wellcome Trust (208385/Z/17/Z) grants. The Astbury cryo-EM facility is funded by a University of Leeds ABSL award and Wellcome Trust grant 108466/Z/15/Z.

Reviewer information *Nature* thanks Tony Huang and the other anonymous reviewer(s) for their contribution to the peer review of this work.

Author contributions M.W. performed electron microscopy experiments, data processing and model building with assistance from E.L.H. and S.K.M. L.T. performed cell-based experiments, immunoprecipitation, challenge assays, metabolic analysis and immunoblots. M.W. and U.M.S. cloned and purified proteins, and performed in vitro interaction studies. R.R. and F.D.G. performed qRT-PCR and gene-expression data analysis. D.P.B. and P.A.E. performed differential scanning fluorimetry assays and data analysis. J.C. performed enzyme kinetics. R.G. and J.R.A. performed mass spectrometry analyses. F.E.O. generated reagents. K.P. performed bioinformatics analyses. J.M.S., P.A.E., F.D.G., N.A.R. and R.A.G. contributed to conception and supervision of experiments. E.Z. performed enzyme assays and conceived and supervised the project. E.Z., M.W., L.T. and R.A.G. wrote the manuscript with input from N.A.R., P.A.E. and F.D.G. All authors critically reviewed the manuscript.

Competing interests F.E.O. declares competing financial interests as co-founder and shareholder of UbiQ Bio BV.

Additional information
Extended data is available for this paper at https://doi.org/10.1038/s41586-019-1232-1.
Supplementary information is available for this paper at https://doi.org/10.1038/s41586-019-1232-1.
Reprints and permissions information is available at http://www.nature.com/reprints.
Correspondence and requests for materials should be addressed to R.A.G. or E.Z.
Publisher's note: Springer Nature remains neutral with regard to jurisdictional claims in published maps and institutional affiliations.

METHODS

No statistical methods were used to predetermine sample size. The experiments were not randomized and investigators were not blinded to allocation during experiments and outcome assessment.

Cloning, protein expression and purification of BRISC–SHMT2 complex and SHMT1. Genes for the four-subunit human BRISC were cloned in the MultiBac system used for co-expression of multiprotein complexes in insect cells (Sf9)[29]. A single 6×His purification tag followed by a cleavable TEV site was engineered at the N terminus of BRCC45. Virus preparation, protein production and protein purification were performed as previously described[13].

Wild-type and mutant forms of human SHMT2ΔN (residues 18–504) and SHMT1 were cloned in a pProEx-HTb vector and expressed in *Escherichia coli* BL21 (DE3) codon plus RIL in Terrific Broth (TB) in the presence of 100 μg/ml ampicillin and 34 μg/ml chloramphenicol at 37 °C to an optical density at 600 nm (OD_{600}) of 1.0–1.2 arbitrary units (AU). Cells were then induced with 0.5 mM isopropyl-1-thio-D-galactopyranoside (IPTG) and incubated overnight at 18 °C. Cells were collected by centrifugation at 5,500*g* and cell pellets were resuspended in lysis buffer (50 mM Tris-HCl, pH 7.6, 300 mM NaCl, 20 mM imidazole, 0.075% β-mercaptoethanol, 5% glycerol, 1 mM benzamidine, 0.8 mM phenylmethyl sulfonyl fluoride (PMSF) and 0.3 mg/ml lysozyme). Cells were lysed by sonication (1-s on, 3-s off for a total of 16 min) on ice and the lysates were cleared by centrifugation at 26,000*g*. The clarified lysate was loaded onto a 5-ml chelating FastFlow column (GE Healthcare), charged with Ni^{2+}. The column was washed with 4 column volumes (CV) of wash buffer consisting of 50 mM Tris-HCl (pH 7.6), 500 mM NaCl, 20 mM imidazole, 0.075% β-mercaptoethanol and 1 mM benzamidine, and the protein was eluted by applying an imidazole gradient with elution buffer consisting of 50 mM Tris-HCl (pH 7.6), 300 mM NaCl, 300 mM imidazole, 0.075% β-mercaptoethanol and 1 mM benzamidine. The fractions containing SHMT2ΔN or SHMT1 were pooled and dialysed against buffer containing 20 mM MES, pH 6.5, 250 mM NaCl, 5% glycerol, 20 mM imidazole, 0.075% β-mercaptoethanol and 1 mM benzamidine. TEV was added to the protein sample and incubated overnight at 4 °C. Dialysed protein was loaded on a 16/600 Superdex200 column (GE Healthcare), equilibrated with 20 mM MES (pH 6.5), 500 mM NaCl and 2 mM TECP.

BRISCΔNΔC and SHMT2ΔN(A285T) were mixed in vitro at 1:4 molar ratio and incubated on ice for 40 min. The mixture was then injected onto a Superdex 10/300 S200 column and peak fractions were analysed by sodium dodecyl sulfate–polyacrylamide gel electrophoresis (SDS–PAGE). Fractions containing the BRISCΔNΔC–SHMT2ΔN(A285T) complex were pooled, and the BRISC–SHMT2ΔN(A285T) complex was used immediately for grid preparation and electron microscopy analysis, as described below. The remaining BRISC–SHMT2ΔN(A285T) complex was pooled and stored at -80 °C at a final concentration of 0.5 mg/ml. Denatured and native masses of all protein preparations were verified by mass spectrometry.

Negative-stain electron microscopy. BRISCΔNΔC and BRISCΔNΔC–SHMT2ΔN(A285T) complexes were diluted in buffer (25 mM HEPES, pH 7.5, 150 mM NaCl, 1 mM TCEP) to 0.0041 mg/ml and 0.0051 mg/ml, respectively, immediately before grid preparation. Glow-discharged, 300-mesh carbon-coated copper grids (Agar Scientific) were incubated with 7 μl BRISCΔNΔC or BRISCΔNΔC–SHMT2ΔN(A285T) for 60 s, passed through 3 droplets of water and stained twice with 2% w/v uranyl acetate for 20 s and 10 s, respectively. Excess liquid was removed by blotting. Micrographs were collected on an FEI Tecnai F20 electron microscope operated at 120 kV equipped with an FEI Ceta CMOS camera. Data processing was carried out using RELION 2.1. Initially, ~1,500 particles were picked manually and extracted with a 450 $Å^2$ box size. Particles were subjected to reference-free 2D classification to generate initial references for auto-picking. A total of 28,566 and 26,824 particles were picked for the BRISCNΔC and BRISCΔNΔC–SHMT2ΔN(A285T) complexes, respectively. One round of reference-free 2D classification was then carried out for each.

Cryo-grid preparation and data collection. BRISCΔNΔC–SHMT2ΔN(A285T) complex was diluted to 0.05 mg/ml in buffer (25 mM HEPES, pH 7.5, 150 mM NaCl, 1 mM TCEP) immediately before grid preparation. Cryo-EM grids were prepared by placing 3 μl of this complex onto glow-discharged, 200-mesh copper grids (Quantifoil R1.2/1.3), followed by immediate blotting and plunge-freezing in liquid ethane cooled by liquid nitrogen, using an FEI Vitrobot IV at 95% relative humidity, chamber temperature of 4 °C. Datasets were collected on an FEI Titan Krios transmission electron microscope at 300 kV, using a total electron dose between 83 and 95 e^- per $Å^2$, a magnification of 75,000× and a final calibrated object sampling of 1.065 Å per pixel. Three independent datasets, giving a total of 7,494 movies, were recorded using the EPU automated acquisition software on an FEI Falcon III direct electron detector[30]. Each exposure movie had a total exposure time of 2 s collected over 70–79 frames with an electron dose of 1.2 e^- per A^2 per frame. Detailed information on data collection is shown in Extended Data Table 1.

Image processing. A schematic of the data processing pipeline is shown in Extended Data Fig. 4. Image processing was carried out using RELION 3.0[31]. Drift-corrected averages of each movie were created using MOTIONCORR2[32] and the contrast transfer function of each determined using gCTF[33]. Initially, ~2,000 particles for each dataset were manually picked, extracted with a box size of 373 $Å^2$ and subjected to reference-free 2D classification to generate initial references for auto-picking. After auto-picking, each dataset was individually subjected to iterative rounds of reference-free 2D classification. Based on visual inspection, quality 2D average classes were selected for each dataset and then the three sets were combined. An initial model generated ab initio from the 2D class averages of the BRISCΔNΔC–SHMT2 negative-stain data, filtered to ~60 Å, was used for initial 3D classification of the combined dataset. Of the eight classes generated, one contained particles comprising the intact complex—that is, the BRCC36–Abraxas 2–SHMT2 core and both BRCC45–MERIT40 arms. This class was processed as a separate dataset consisting of 71,262 particles, representing the complete, two-arm structure. In parallel, this class—along with four others (totalling 514,930 particles)—was processed to represent the complete dataset. Both were subjected to a final round of 3D classification to remove any remaining 'bad' particles. The best classes from 3D classification were taken forward and subjected to 3D refinement, per-particle CTF correction and particle polishing[31]. C2 symmetry was imposed to the two-arm dataset. Post-processing was used to appropriately mask the model, estimate and correct for the B-factor of the maps. Final resolutions were determined using the gold-standard Fourier shell correlation criterion (FSC = 0.143). Local resolution was estimated using the local resolution feature in RELION.

Model building and refinement. A preliminary model for the BRISCΔNΔC–SHMT2ΔN(A285T) complex was generated using a combination of known crystal structures (BRCC36–Abraxas 2 superdimer from *Camponotus floridanus* (PDB code 5CW3) and human SHMT2 dimer (PDB code 6DK3)) and homology models generated by Phyre2[34] (BRCC45, consisting of two UEV domains, and MERIT40). This initial model was manually fitted into the electron microscopy density map for the C1 reconstruction (3.8 Å) using rigid-body fitting in UCSF Chimera[35]. The model was then manually fitted and rebuilt in COOT[36] to trace the human sequences of BRCC36 and Abraxas 2. Amino acid residues that lacked unambiguous density were deleted or modelled up to their Cβ position while preserving sequence information. The Cα backbone for BRCC45 UEV-N and UEV-M was traced into the remaining density mainly as alanine and glycine residues, and the precise sequence for BRCC45 could not be modelled with confidence. Gaps numbered arbitrarily were left where direct connectivity between secondary structure elements could not be determined.

The higher-resolution C1 map was used for model building and the two-arm model was generated by using the two-fold symmetry of the superdimer core.

The model was refined against the C1 and C2 maps in Phenix[37] using default parameters and secondary structure restraints. The overall quality of the model was assessed using MolProbity[38]. Fitting of the remaining BRCC45 UEV-C and MERIT40 domains into the peripheral parts of the C2 electron microscopy map was carried out using rigid-body fitting in Chimera; these are displayed for relative position and size comparison purposes only.

DUB activity assays. BRISC complexes were assayed at 30 °C in DUB reaction buffer containing 50 mM HEPES-NaOH pH 7.0, 100 mM NaCl, 0.1 mg/ml BSA, 1 mM DTT and 0.005% Tween-20. Internally quenched fluorescent (IQF) K63-linked diUb (Lifesensors, catalogue number: DU6303) was used as a reporter for DUB activity (1 part IQF diUB to 9 parts unlabelled K63-linked diUb, prepared as previously described[39]). Twenty-microlitre enzyme reactions were carried out in 384-well black flat-bottom low-flange plates (Corning; 35373). Cleaved diUb was monitored by measuring fluorescence intensity (excitation, 540 nm; emission, 580 nm; dichroic mirror, 560 nm) every 1 min over 20 min, and initial velocity (v_o) was calculated as the slope of the linear part of the reaction-progress curve. Fluorescence intensity units were converted to nM product concentration using TAMRA-labelled ubiquitin (Lifesensors, catalogue number: SI270T) as a standard. Enzyme concentrations for which a reasonable progress curve was obtained over 20 min were: 1 nM BRISC and 40 nM ARISC. Substrate concentration was 300 nM. IC_{50} values were calculated by fitting the data using the GraphPad Prism built-in dose–response equation for inhibition with variable slope: $y = \text{bottom} + (\text{top} - \text{bottom}) / (1 + 10^{((\log(IC_{50}) - x) \times h)})$. Michaelis–Menten analysis in the absence and presence of increasing concentrations of SHMT2 was performed in DUB buffer containing 50 mM HEPES-NaOH (pH 6.8), 100 mM NaCl and 5 mM DTT. BRISC concentration was 1.5–2.0 nM and IQF K63-linked diUb was used (0–4 μM) as substrate (concentrations greater than 4 μM inhibited BRISC activity). Data were fit using the standard Michaelis–Menten equation, constraining V_{max} to be less than the V_{max} in the absence of SHMT2. Lineweaver–Burk plots and Michaelis–Menten analysis were performed using GraphPad Prism.

K63-linked hexaUb chains were also used to determine DUB activity. Sixty-microlitre reactions were carried out in 1.5 ml Eppendorf tubes at 30 °C in DUB reaction buffer. BRISC was incubated in the presence or absence of

SHMT2ΔN or SHMT1 forms for 30 min at room temperature, before the addition of hexaUb(K63). Reactions containing 0.5 nM BRISC, 2 μM SHMT and 1 μM hexaUb(K63) were incubated for 1 h. Immunoblotting was performed with commercially available HRP-conjugated antibody to Ub (P4D1, Santa Cruz).

SHMT2 PLP association and enzyme activity assays. PLP association assays were performed in 20-μl reactions in 384-well plates (Greiner) in buffer containing 50 mM HEPES-Na (pH 7.8), 50 mM NaCl, 50 mM KCl, 5% glycerol, 0.2 mM DTT, 0.1 mM EDTA and 0.005% Tween-20. SHMT2ΔN and point mutants (5 μM) were rapidly mixed with PLP (100 μM) and the reaction was monitored by measuring absorbance at 435 nm (every 30 s over 1 h) using a Hidex Sense microplate reader.

SHMT2ΔN enzyme activity was monitored in 20-μl reactions in 384-well, UV-transparent plates (Greiner). The synthetic substrate L-threo-phenylserine (2S,3R)-2-amino-3-hydroxy-3-phenylpropionic acid (BACHEM) was used as previously described[40] with minor modifications. Reactions were performed in buffer containing 50 mM HEPES-Na (pH 7.5), 100 mM NaCl, 0.5 mM TCEP and 0.005% Tween-20. SHMT2ΔN and point mutants (2 μM) were preincubated with 200 μM PLP for 1 h at 25 °C. Five microlitres of enzyme–PLP solution was added to 15 μl of solution containing 0–260 mM L-threo-phenylserine, and the reaction was monitored by measuring absorbance of benzyldehyde at 279 nm in a Hidex Sense microplate reader (every 2 min over 20 min). Absorbance units were converted to molar concentrations using a standard curve of known concentrations of benzyldehyde solutions (Sigma). Initial velocity (v_o) was calculated as the slope of the linear part of the reaction progress curve (20 min).

Differential scanning fluorimetry. Thermal-shift assays were performed using an Applied Biosystems StepOnePlus Real-Time PCR instrument and a standardized differential scanning fluorimetry procedure[41]. Proteins were diluted in 50 mM Tris-HCl (pH 7.4) and 100 mM NaCl to a concentration of 5 μM, and then incubated with the indicated concentration of compound in a total reaction volume of 10 μl, with final concentration of 2% (v/v) DMSO. SYPRO Orange (Invitrogen) was used as a fluorescence probe. The temperature was raised in regular 0.3-°C intervals from 25 °C to 95 °C. Compound binding experiments were assessed in duplicate and reported relative to DMSO controls. Normalized data were processed using the Boltzmann equation to generate sigmoidal denaturation curves, and $T_m/\Delta T_m$ values were calculated as previously described[41].

Native mass spectrometry. BRISCΔNΔC–SHMT2ΔN(A285T) (2.6 μM) and SHMT2ΔN and various mutants (2–20 μM) were buffer-exchanged into 0.2–1 M ammonium acetate (pH 7.2) using Zeba Spin 7K MWCO desalting columns (ThermoFisher). Samples were analysed by nano-electrospray ionization mass spectrometry using either a quadrupole-IMS-orthogonal time-of-flight (TOF) mass spectrometer (Synapt HDMS, Waters UK), operated as previously described[42], or a quadrupole orbitrap mass spectrometer modified for transmission of high m/z ions (Q-Exactive Plus, ThermoScientific), operated as previously described[43,44]. Both used gold- and palladium-coated nanospray tips prepared in-house. Data from the Synapt were processed using the MassLynx v4.1 suite of software supplied with the mass spectrometer, and UniDec v2.7.1[45]. Data from the Q-Exactive Plus were processed using Xcalibur Qual Browser v4.0.27.19 and UniDec v2.7.1.

Analytical size-exclusion chromatography. Full-length BRISC and SHMT2ΔN or SHMT1 forms were mixed in vitro at 1:1 molar ratio (~6 μM) and incubated on ice for 30 min. The mixture was then injected onto a 2.4-ml Superose 6 analytical size-exclusion column. Peak fractions were analysed by SDS–PAGE. Controls for each protein were also run.

Immunoprecipitation and immunoblots. All immunoprecipitations were performed as previously described[46]. In brief, BRCC36- and Abraxas-2-expressing cells were lysed in NETN 150 (0.5% NP40, 25 mM Tris pH 7.5, 150 mM NaCl, 0.5 mM EDTA with 1mM PMSF). Flag immunoprecipitations were performed on lysate supernatants for 4 h with agarose-conjugated anti-Flag M2 beads (Sigma) before elution in 0.1 mM glycine (pH 2.5). Immunoblots were performed with the following rabbit polyclonal antibodies at 1:1,000 dilution that were generated to recombinant proteins: MERIT40, Abraxas 2, BRCC36 and BRCC45. Commercially available antibodies to the HA epitope (HA.11 Covance) and SHMT2 (Cell Signaling) were used according to the manufacturer's directions. An Abraxas 2 deletion mutant (DM1) was used as control, as previously described[12].

For assessment of IFNAR1 ubiquitylation in cells, cells were lysed in buffer containing 2% SDS, 150 mM NaCl, 10 mM Tris-HCl, pH 8.0, 50 mM sodium fluoride, 10mM *N*-ethylmaleimide and protease inhibitors. After boiling for 10 min, cell lysates were further diluted in immunoprecipiation buffer (10 mM Tris-HCl, pH 8.0, 150 mM NaCl, 2 mM EDTA, 1% Triton X-100). IFNAR1 was immunoprecipitated with a corresponding antibody (Bethyl Laboratories A304-290A). Resulting samples were separated by SDS–PAGE and analysed by immunoblotting using the anti-ubiquitin antibody (Lifesensor, VU101).

Response to HSV infection, LPS and IFNβ. HSV lacking the *ICP0* gene was used to infect cells at a multiplicity of infection of 0.1 for 2 h. Medium was then changed followed by a 5-h incubation period. Cells were then lysed in NETN150 and lysates were run on a 4–12% gradient SDS–PAGE gel for immunoblot. Phosphorylated STAT1 and STAT1 antibodies were purchased from Cell Signaling Corporation and used according to the manufacturer's specifications. Monitoring of phosphorylated STAT1 after LPS or IFNβ treatment was performed using conditions similar to those previously described[12].

Cellular PLP level manipulation and validation. MEFs or HEK293T cells were cultured in B6 vitamer-free Dulbecco's modified Eagle's medium (DMEM, from Gibco), B6-vitamer-free DMEM + 20 μmol/l pyridoxal hydrochloride (Sigma) or B6-vitamer-free DMEM + 50 μmol/l pyridoxal hydrochloride. All medium was supplemented with 10% FBS. After 48 h of culture, cells were collected and snap-frozen in liquid nitrogen. Pyridoxal, pyridoxal phosphate and pyridoxine levels were measured using liquid chromatography–mass spectrometry as previously described[47].

qRT–PCR analysis of gene expression in MEFs. IFN-type I-related gene expression was analysed in *Abraxas2*$^{-/-}$ MEFs after treatment with LPS or vehicle control. Gene expression was performed in *Abraxas2*$^{-/-}$ MEFs and compared to derivative lines that had been stably reconstituted with Abraxas 2 wild type or mutant E144R using retroviral transduction. Following 16 h of LPS exposure, cells were directly lysed in TRIzol (Thermo Fisher Scientific) and RNA was extracted using Quick-RNA Miniprep Kit (Zymo Research) as per the manufacturer's instructions. Four hundred nanograms of eluted RNA was converted to cDNA using RT2 First Strand Kit (Qiagen). Next, the cDNA was mixed with RT2 SYBR Green Mastermix (Qiagen). The mouse IFN I RT2 Profiler PCR Array (Qiagen cat. no. PAMM-016Z) was performed and relative expression determined using the $\Delta\Delta C_t$ method and normalized for four housekeeping genes according to manufacturer's guidance. Single measurements of three biological repeats were performed. Total results were analysed and compared to the gene signature of *Abraxas2*$^{-/-}$ MEFs, with and without LPS treatment. Gene-expression analysis of MEFs cultured in B6-vitamer-free DMEM with and without 20 μM pyridoxal hydrochloride was performed as above.

Reporting summary. Further information on research design is available in the Nature Research Reporting Summary linked to this paper.

Data availability

Coordinates have been deposited in the Protein Data Bank, code 6R8F. Cryo-EM reconstructions in C1 and C2 have been deposited in the Electron Microscopy Data Bank, codes EMD-4759 and EMD-4760. Any other relevant data are available from the corresponding authors upon reasonable request.

29. Fitzgerald, D. J., et al. Protein complex expression by using multigene baculoviral vectors. *Nat. Methods* **3**, 1021–1032 (2006).
30. Thompson, R. F., Iadanza, M. G., Hesketh, E. L., Rawson, S. & Ranson, N. A. Collection, pre-processing and on-the-fly analysis of data for high-resolution, single-particle cryo-electron microscopy. *Nat. Protocols* **14**, 100–118 (2019).
31. Zivanov, J. et al. New tools for automated high-resolution cryo-EM structure determination in RELION-3. *eLife* **7**, e42166 (2018).
32. Zheng, S. Q., et al. MotionCor2: anisotropic correction of beam-induced motion for improved cryo-electron microscopy. *Nat. Methods* **2006 3:12 14**, 331–332 (2017).
33. Zhang, K. Gctf: Real-time CTF determination and correction. *J. Struct. Biol.* **193**, 1–12 (2016).
34. Kelley, L. A., Mezulis, S., Yates, C. M., Wass, M. N. & Sternberg, M. J. E. The Phyre2 web portal for protein modeling, prediction and analysis. *Nat. Protocols* **10**, 845–858 (2015).
35. Pettersen, E. F. et al. UCSF Chimera—a visualization system for exploratory research and analysis. *J. Comput. Chem.* **25**, 1605–1612 (2004).
36. Emsley, P., Lohkamp, B., Scott, W. G. & Cowtan, K. Features and development of Coot. *Acta Crystallogr. D* **66**, 486–501 (2010).
37. Adams, P. D. et al. PHENIX: a comprehensive Python-based system for macromolecular structure solution. *Acta Crystallogr. D* **66**, 213–221 (2010).
38. Chen, V. B. et al. MolProbity: all-atom structure validation for macromolecular crystallography. *Acta Crystallogr. D* **66**, 12–21 (2010).
39. Pickart, C. M. & Raasi, S. Controlled synthesis of polyubiquitin chains *Methods Enzymol.* **399**, 21–36 (2005).
40. Wei, Z. et al. Deacetylation of serine hydroxymethyl-transferase 2 by SIRT3 promotes colorectal carcinogenesis. *Nat Commun.* **9**, 4468 (2018).
41. Byrne, D. P. et al. cAMP-dependent protein kinase (PKA) complexes probed by complementary differential scanning fluorimetry and ion mobility-mass spectrometry. *Biochem. J.* **473**, 3159–3175 (2016).
42. Scarff, C. A. et al. Examination of ataxin-3 (atx-3) aggregation by structural mass spectrometry techniques: a rationale for expedited aggregation upon polyglutamine (polyQ) expansion. *Mol. Cell. Proteomics* **14**, 1241–1253 (2015).
43. Gault, J., et al. High-resolution mass spectrometry of small molecules bound to membrane proteins. *Nat. Methods* **13**, 333–336 (2016).
44. Rose, R. J., Damoc, E., Denisov, E., Makarov, A. & Heck, A. J. R. High-sensitivity Orbitrap mass analysis of intact macromolecular assemblies. *Nat. Methods* **9**, 1084–1086 (2012).
45. Marty, M. T. et al. Bayesian deconvolution of mass and ion mobility spectra: from binary interactions to polydisperse ensembles. *Anal. Chem.* **87**, 4370–4376 (2015).
46. Shao, G. et al. MERIT40 controls BRCA1–Rap80 complex integrity and recruitment to DNA double-strand breaks. *Genes Dev.* **23**, 740–754 (2009).
47. Ochocki, J. D. et al. Arginase 2 suppresses renal carcinoma progression via biosynthetic cofactor pyridoxal phosphate depletion and increased polyamine toxicity. *Cell Metab.* **27**, 1263–1280.e6 (2018).

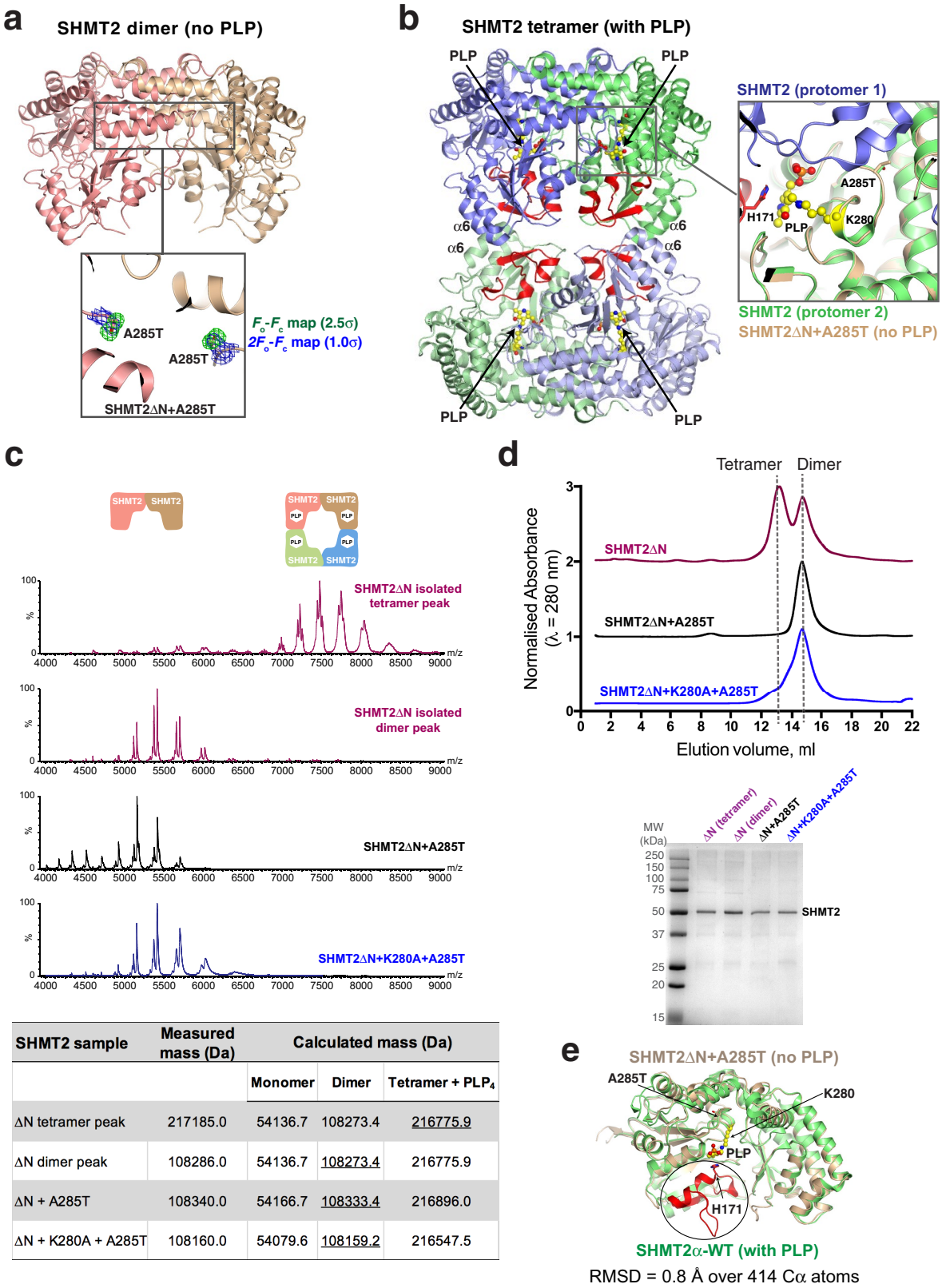

SHMT2 sample	Measured mass (Da)	Calculated mass (Da)		
		Monomer	Dimer	Tetramer + PLP_4
ΔN tetramer peak	217185.0	54136.7	108273.4	216775.9
ΔN dimer peak	108286.0	54136.7	108273.4	216775.9
ΔN + A285T	108340.0	54166.7	108333.4	216896.0
ΔN + K280A + A285T	108160.0	54079.6	108159.2	216547.5

Extended Data Fig. 1 | SHMT2 exists in a dimer–tetramer equilibrium. **a**, Structure of SHMT2ΔN(A285T) dimer (PDB code 6DK3). Unbiased electron density maps are coloured green. The structure was erroneously deposited by the Structural Genomics Consortium (SGC) as wild type with PDB code 3OU5. It was corrected and redeposited with PDB code 6DK3 on 28 May 2018. **b**, Structure of wild-type SHMT2α tetramer (PDB code 4PVF) bound to PLP. Regions in red show structural rearrangements upon PLP binding. **c**, Native mass spectrometry spectra (single measurement experiment) of different forms of SHMT2ΔN (top) and measured and calculated masses (bottom). Calculated masses nearest to the measured masses are underlined. **d**, Size-exclusion chromatography profiles of different forms of SHMT2ΔN (top) and a Coomassie-stained SDS–PAGE gel (bottom). Data are representative of three independent experiments. **e**, Comparison of SHMT2 protomers with and without PLP.

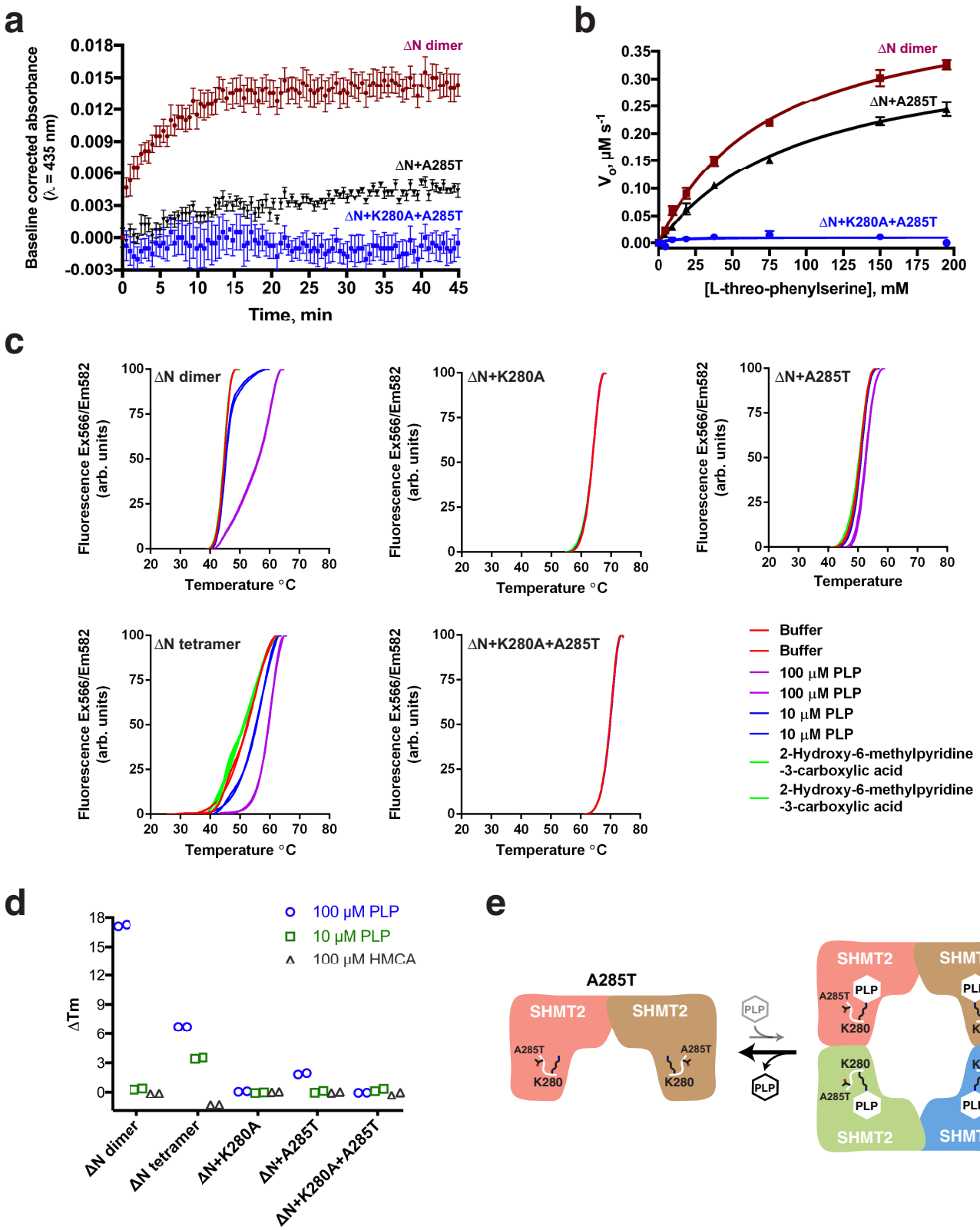

Extended Data Fig. 2 | PLP regulates SHMT2 dimer-tetramer transition. a, PLP association with the indicated forms of SHMT2ΔN. SHMT2–PLP internal aldimine linkage was monitored by measuring absorbance at 435 nm after rapid mixing of SHMT2ΔN (5 μM) and PLP (100 μM). Data are mean ± s.e.m. of four independent reactions. **b**, Enzyme activity of the indicated forms of SHMT2ΔN (0.5 μM) against the synthetic substrate L-threo-phenylserine in the presence of 50 μM PLP. The reaction was monitored by measuring benzyldehyde absorbance at 279 nm. Data are mean ± s.e.m. of three independent experiments carried out in duplicate. **c**, Differential scanning fluorimetry analysis of different forms of SHMT2ΔN in the presence and absence of PLP. SHMT2ΔN wild-type and mutant proteins (5 μM) were incubated with the indicated concentrations of PLP or 100 μM 2-hydroxy-6-methylpyridine-3-carboxylic acid (HMCA) for 10 min at 20 °C before differential scanning fluorimetry analysis. **d**, Changes in melting temperatures (ΔT_m) for each of the conditions shown in **c**. ΔT_m was calculated by subtracting the T_m of SHMT2 with buffer without ligands from the T_m of SHMT2 with added ligands. Data in **c**, **d** represent a single experiment carried out in duplicate. **e**, Summary of SHMT2ΔN(A285T) dimer–tetramer equilibrium in response to PLP binding.

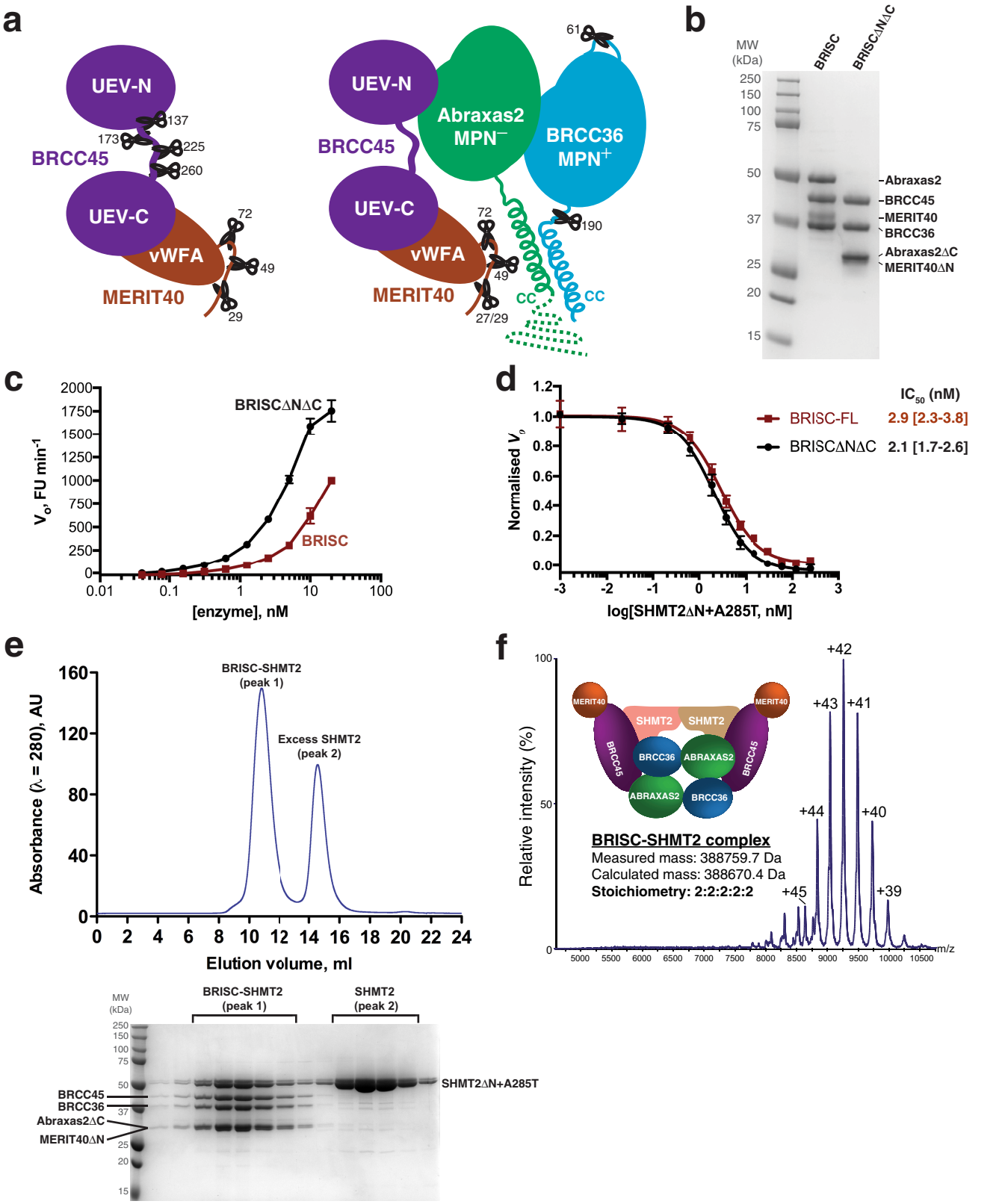

Extended Data Fig. 3 | Reconstitution of BRISC–SHMT2 complex. **a**, Summary of limited proteolysis and Edman sequencing results indicating trypsin protease-labile regions for the BRCC45–MERIT40 complex (left) and the BRISC (right). Protease cleavage sites are shown as scissors. Unstructured Abraxas 2 regions are indicated as dashed lines. **b**, SDS–PAGE of BRISC and BRISCΔNΔC (representative of three independent experiments). **c**, DUB activity of BRISC (full length) and BRISCΔNΔC (truncated) against a fluorogenic K63-linked diUb substrate. Data are mean ± s.e.m. of three independent experiments carried out in duplicate. **d**, SHMT2ΔN(A285T) inhibition of BRISC and BRISCΔNΔC DUB activity. Data are mean ± s.e.m. of three independent experiments carried out in duplicate. Ninety-five per cent confidence intervals are shown in square brackets. **e**, Size-exclusion chromatography of the BRISCΔNΔC–SHMT2ΔN(A285T) complex (top) and Coomassie-stained SDS–PAGE of peak fractions (bottom). **f**, Native mass spectrometry of the BRISCΔNΔC–SHMT2ΔN(A285T) complex. Data in **e**, **f** are representative of three independent experiments.

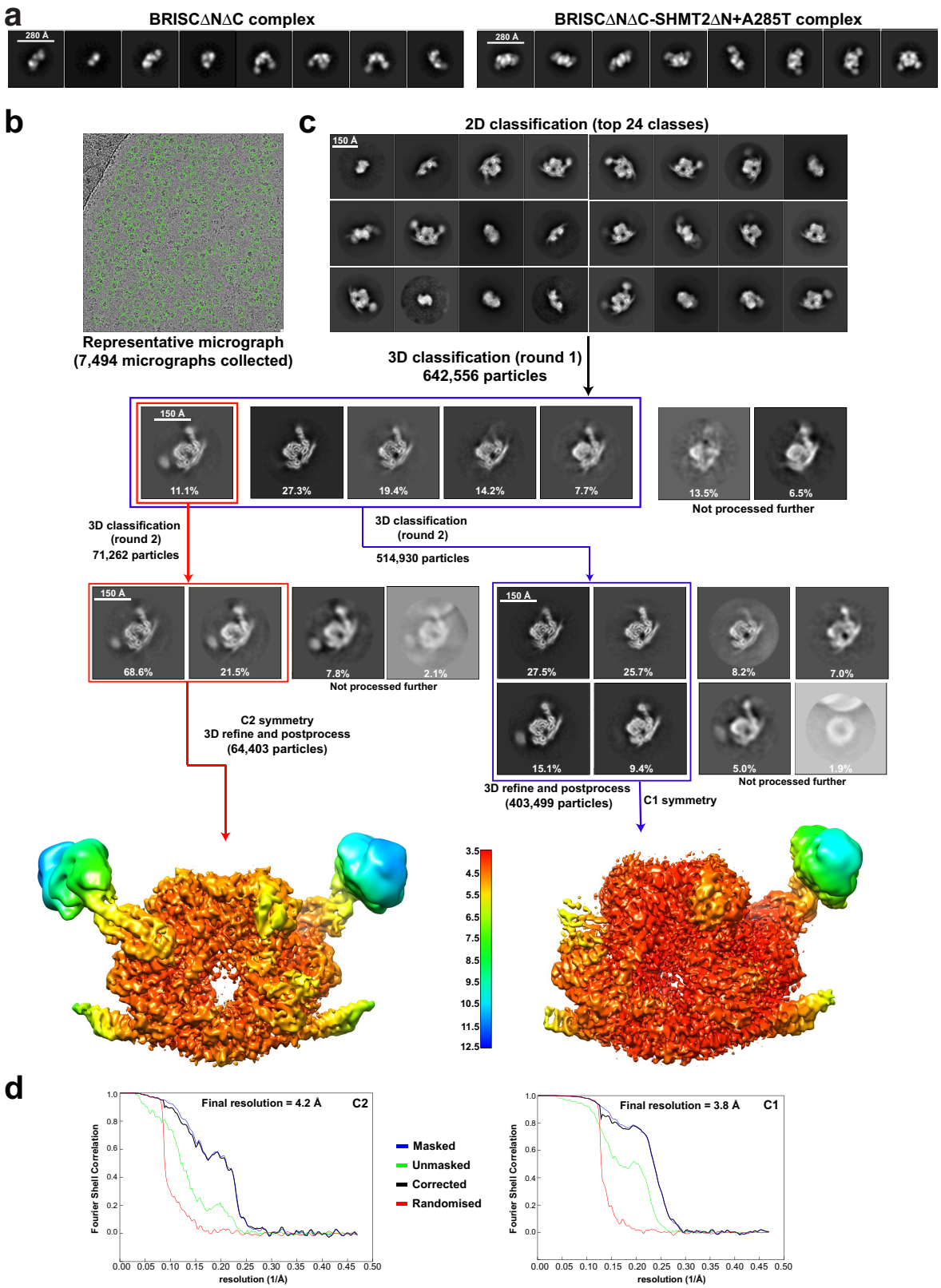

Extended Data Fig. 4 | Electron microscopy analysis of BRISC and BRISC–SHMT2 complex. a, Negative-stain electron microscopy analysis. Selected 2D-averaged classes of BRISCΔNΔC (left) and BRISCΔNΔC–SHMT2ΔN(A285T) (right). **b**, Representative cryo-EM micrograph. Green circles (180 Å diameter) indicate auto-picked particles. **c**, Flow chart of data processing. Final electron microscopy maps, coloured according to local resolution, are provided (scale bar in Å). **d**, FSC curves for the indicated maps. The final resolution was calculated using the gold-standard FSC cut-off at 0.143 frequency.

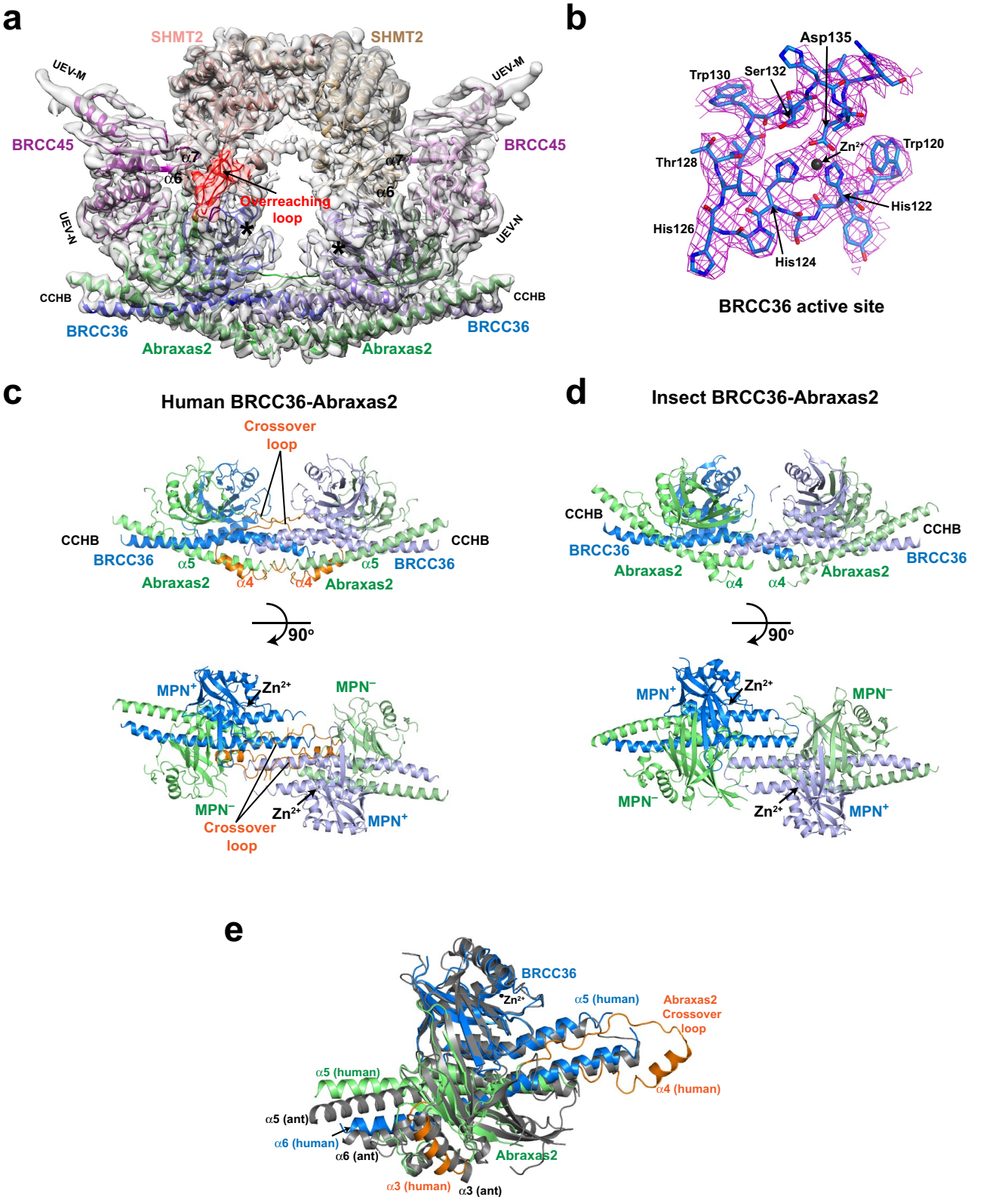

Extended Data Fig. 5 | Structural analysis of BRISC–SHMT2 structures. **a**, Structural overview of the BRISCΔNΔC–SHMT2 structure and cryo-EM maps at a contour level of 0.085 (C2 map), showing secondary structure features. BRCC45 UEV-C and MERIT40 vWFA domains are omitted. CCHB, coiled-coil helical bundle. Asterisks mark the position of the BRCC36 active site. An overreaching loop (SHMT2 residues 296–307) is coloured red. **b**, Representative electron microscopy map of the BRCC36 active site. **c**, **d**, Structure of human (**c**) and insect (*C. floridanus*) (**d**) BRCC36–Abraxas 2 superdimer, highlighting differences and similarities. The connectivity of the MPN$^-$ domain of Abraxas 2 and α4 helix by a crossover loop is different in the insect and human complexes, and is coloured orange in the latter structure. **e**, Superimposition of the BRCC36 MPN$^+$ domain from the insect (grey) and human (blue, green) heterodimers. Abraxas-2 regions with notable differences between the two structures are coloured orange.

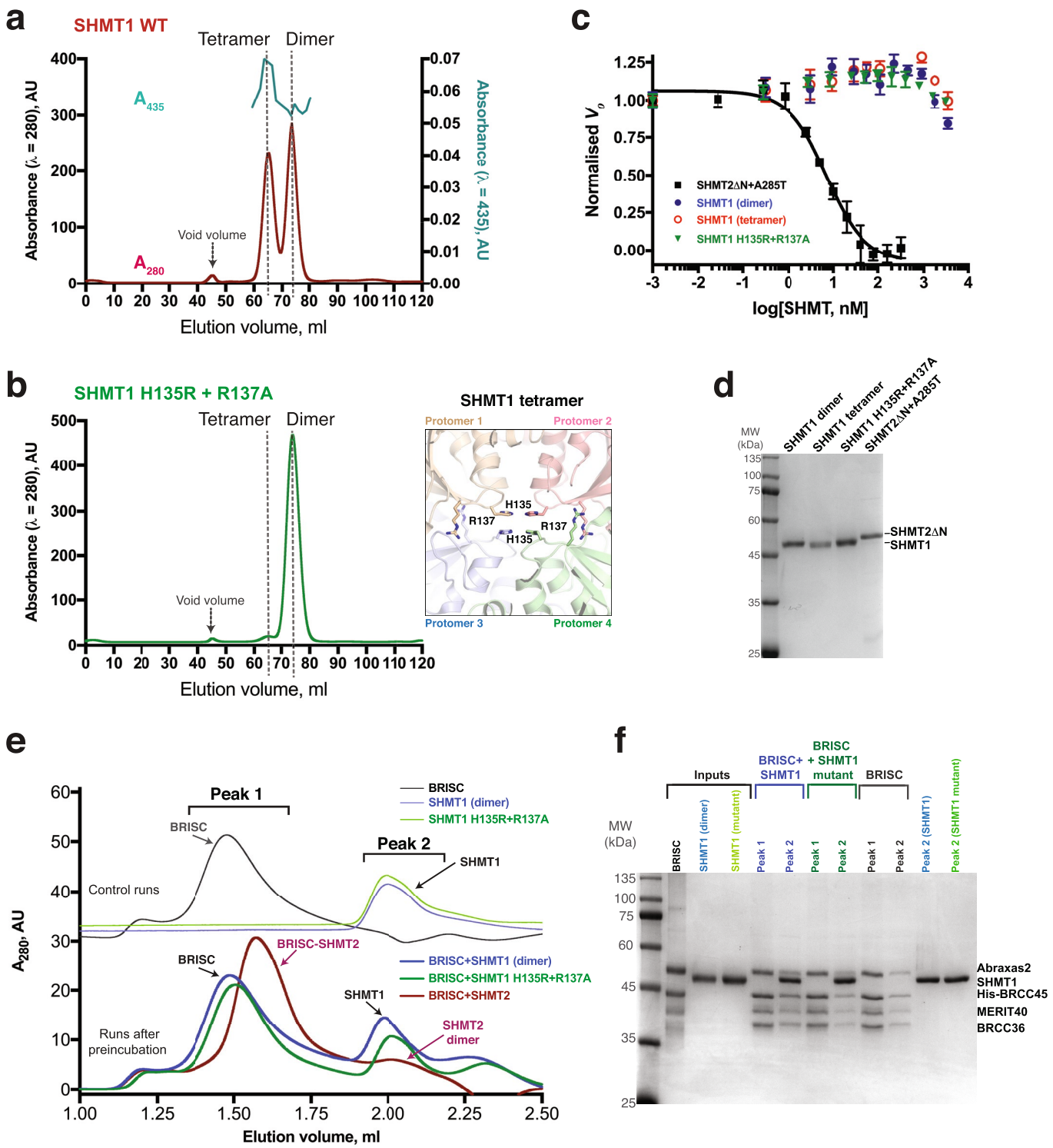

Extended Data Fig. 6 | Analysis of SHMT1 interaction with BRISC. **a**, Elution profile of wild-type SHMT1 from an S75 16/600 size-exclusion chromatography column (data are representative of two independent experiments). **b**, Elution profile of SHMT1 containing mutated residues designed to break the tetrameric interface (left; data are from a single experiment). Structure of SHMT1 tetramer (PDB code 1RV4), highlighting residues that are important for tetramerization (right). **c**, BRISC DUB activity against a fluorogenic K63-linked diUb substrate in the presence of the indicated forms of SHMT1 and SHMT2. Data are mean ± s.e.m. of three independent experiments carried out in duplicate. For gel source data, see Supplementary Fig. 1. **d**, Coomassie-stained SDS–PAGE analysis of the indicated SHMT1 and SHMT2 protein preparations (data are from a single experiment). **e**, Analytical size-exclusion chromatography runs of the indicated protein preparations. SHMT1 proteins were mixed with BRISC for 30 min before injecting on a 2.4-ml Superose 6 column (bottom traces). Traces on top are control runs. A BRISC–SHMT2ΔN run is shown for comparison (see Extended Data Fig. 8e for detailed analysis). **f**, Coomassie-stained SDS–PAGE analysis of the indicated peak fractions from size-exclusion runs shown in **e**. Data in **e**, **f** are representative of two independent experiments.

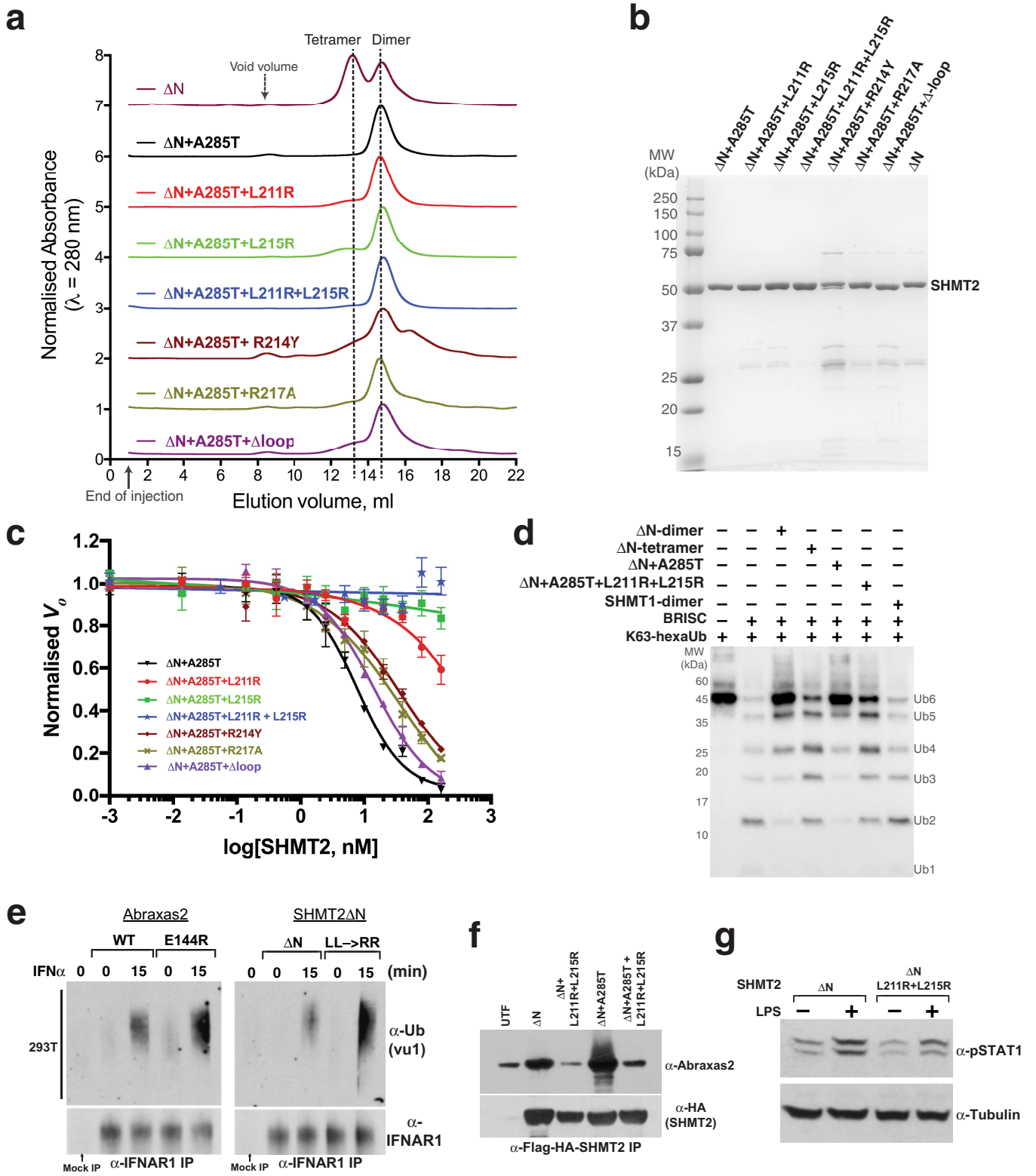

Extended Data Fig. 7 | See next page for caption.

Extended Data Fig. 7 | Purification and analysis of SHMT2 mutants. **a**, Elution profile of the indicated forms of SHMT2ΔN from an S75 10/300 size-exclusion chromatography column (single experiment). **b**, Coomassie-stained SDS–PAGE analysis of the indicated SHMT2ΔN protein preparations (data are representative of two independent experiments). **c**, BRISC DUB activity against a fluorogenic K63-linked diUb substrate in the presence of the indicated SHMT2ΔN mutants. Data are mean ± s.e.m. of three independent experiments carried out in duplicate. **d**, BRISC DUB activity against K63-linked hexaUb chains in the presence of the different forms of SHMT2ΔN, or SHMT1. **e**, Ubiquitylation levels of IFNAR1 after IFNα stimulation in HEK293T cells that overexpress the indicated forms of Abraxas 2 and SHMT2ΔN. The annotation 'LL->RR' denotes SHMT2ΔN(L211R/L215R). IFNAR1 immunoprecipitation (IP) was performed under denaturing conditions and ubiquitin levels were detected using the vu-1 antibody. Mock IP was performed using a generic rabbit IgG antibody. **f**, Immunoprecipitation (IP) performed using anti-Flag antibody in MEFs that were transiently transfected with Flag–HA epitope-tagged SHMT2ΔN or mutants. Immunoblot was performed for Abraxas 2 and SHMT2, as indicated. UTF, untransfected cells (used as control). **g**, MEFs that overexpress the indicated SHMT2ΔN or mutants were challenged with LPS, and interferon-receptor-dependent signal transduction response was assessed by immunoblot for STAT1 phosphorylated at Y701. Data shown in **d**, **e** are representative of three independent experiments. For gel source data, see Supplementary Fig. 1.

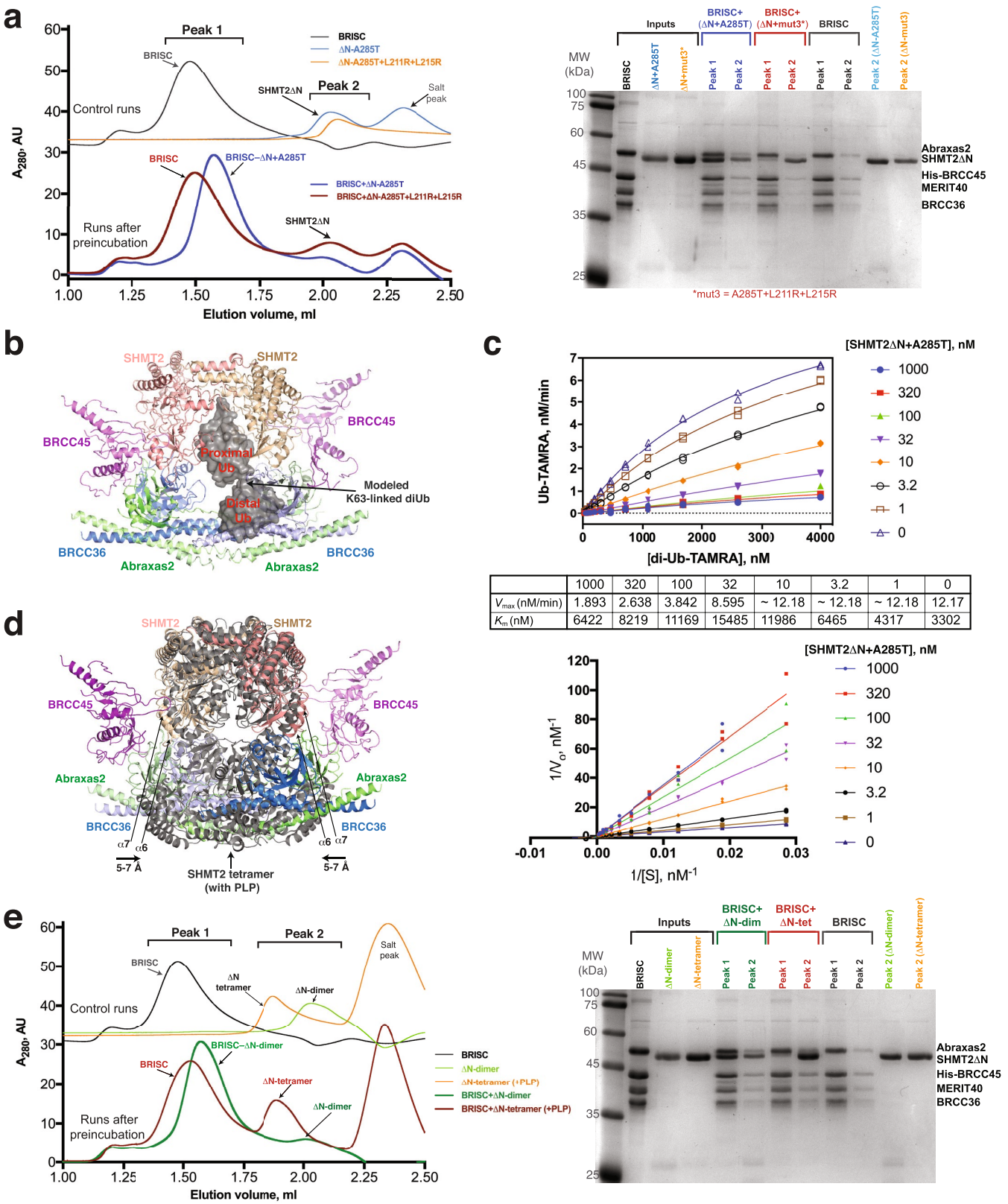

	1000	320	100	32	10	3.2	1	0
V_{max} (nM/min)	1.893	2.638	3.842	8.595	~ 12.18	~ 12.18	~ 12.18	12.17
K_m (nM)	6422	8219	11169	15485	11986	6465	4317	3302

Extended Data Fig. 8 | See next page for caption.

Extended Data Fig. 8 | SHMT2 blocks the BRISC active site. **a**, Analytical size-exclusion chromatography of different forms of SHMT2ΔN, preincubated with BRISC (left) and SDS–PAGE analysis of peak fractions (right). Data are representative of two independent experiments. **b**, K63-linked diUb (grey) modelled on the MPN^+ domain of BRCC36 using the AMSH-LP–diUb structure (PDB code 2ZNV) as a guide. The SHMT2 obligate dimer sterically clashes with the modelled proximal ubiquitin. **c**, Michaelis–Menten (top) and Lineweaver–Burk (bottom) plots for BRISC DUB activity against a K63-linked diUb fluorogenic substrate with addition of SHMT2ΔN(A285T). Technical duplicates are shown and data are representative of two independent experiments. **d**, Superimposition of SHMT2 dimer and tetramer forms. The SHMT2 obligate dimer from the PLP-bound tetramer structure (PDB code 4PVF, coloured grey) was overlaid on the SHMT2ΔN(A285T) dimer bound to BRISC. The second obligate dimer from the SHMT2-–PLP holoenzyme sterically clashes with the BRCC36–Abraxas 2 superdimer. Movement of α6 and α7 helices is indicated. **e**, Analytical size-exclusion chromatography of SHMT2ΔN dimer and tetramer (+PLP) forms with BRISC (left) and SDS–PAGE analysis of peak fractions (right). Data are representative of two independent experiments.

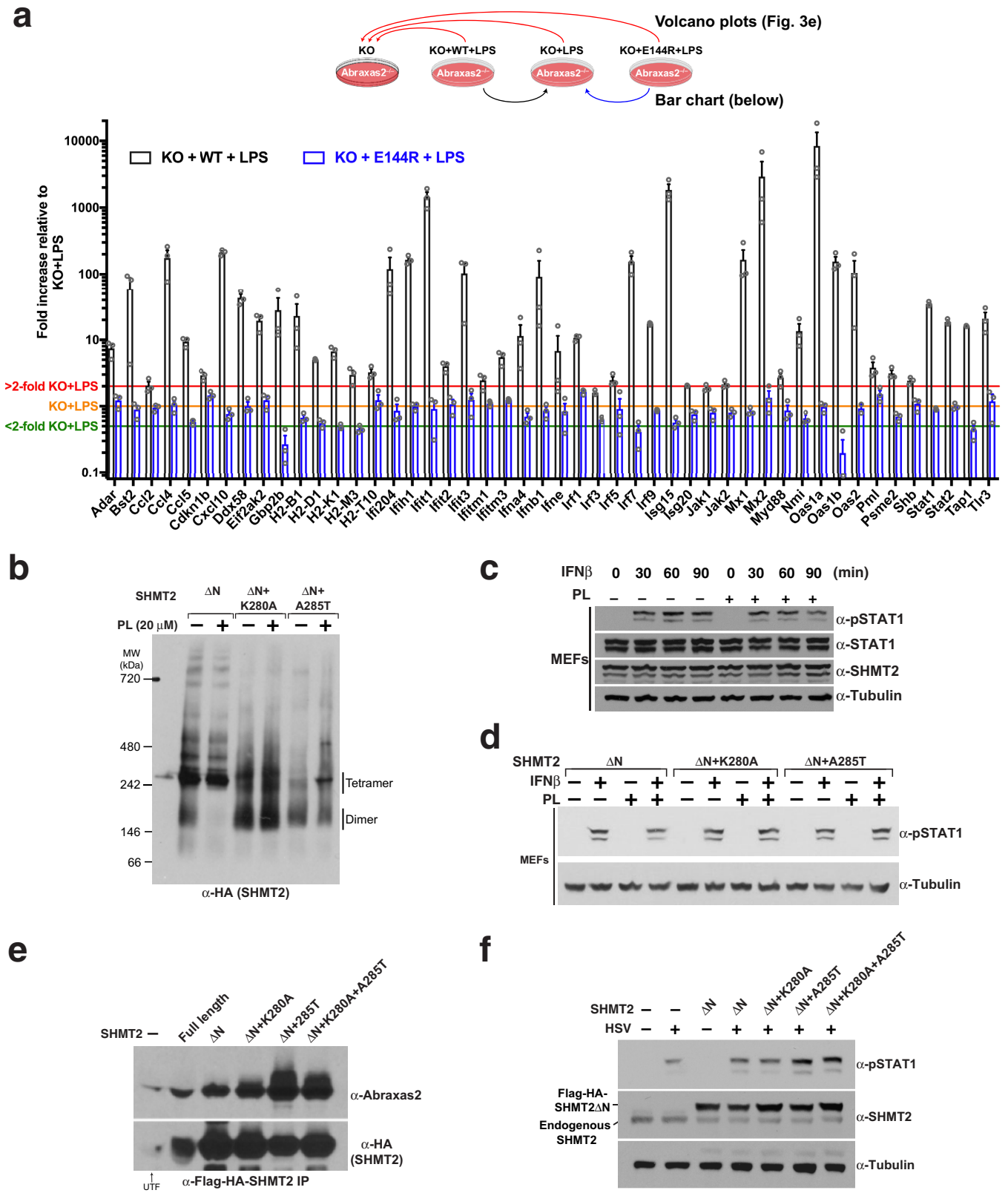

Extended Data Fig. 9 | See next page for caption.

Extended Data Fig. 9 | Regulation of BRISC–SHMT2 function in cells. **a**, Schematic of pairwise comparison of *Abraxas2*$^{-/-}$ MEFs treated with LPS and expressing the indicated forms of Abraxas 2 (top). Bar chart illustrates the IFN-type I-related genes that were increased by more than twofold in Abraxas 2 wild-type + LPS (black) and Abraxas 2(E144R) + LPS (blue), relative to *Abraxas2*$^{-/-}$ + LPS. Data are presented as mean ± s.e.m. from three independent experiments (biological replicates). **b**, Native gel electrophoresis of whole MEF cell lysates cultured in B6-vitamer-free medium, with and without pyridoxal, and expressing the indicated forms of Flag–HA–SHMT2ΔN. **c**, **d**, Measurement of phosphorylated STAT1 levels (phosphorylated at Y701) in MEFs (**c**) or MEFs that stably express SHMT2 (**d**), cultured in B6-vitamer-free medium. Where indicated, cells were treated with 20 μM pyridoxal and/or 500 units per millilitre of IFNβ for 48 h. **e**, Immunoprecipitation performed using anti-Flag antibody in MEFs transiently transfected with Flag–HA epitope-tagged SHMT2 or mutants (cultured in DMEM). Immunoblot was performed for Abraxas 2 and SHMT2 as indicated. **f**, Phosphorylated STAT1 levels (phosphorylated at Y701) measured in MEFs cultured in DMEM containing vitamin B6 and the indicated forms of SHMT, after challenge with HSV. Data shown in **b**–**f** are representative of three independent experiments. For gel source data, see Supplementary Fig. 1.

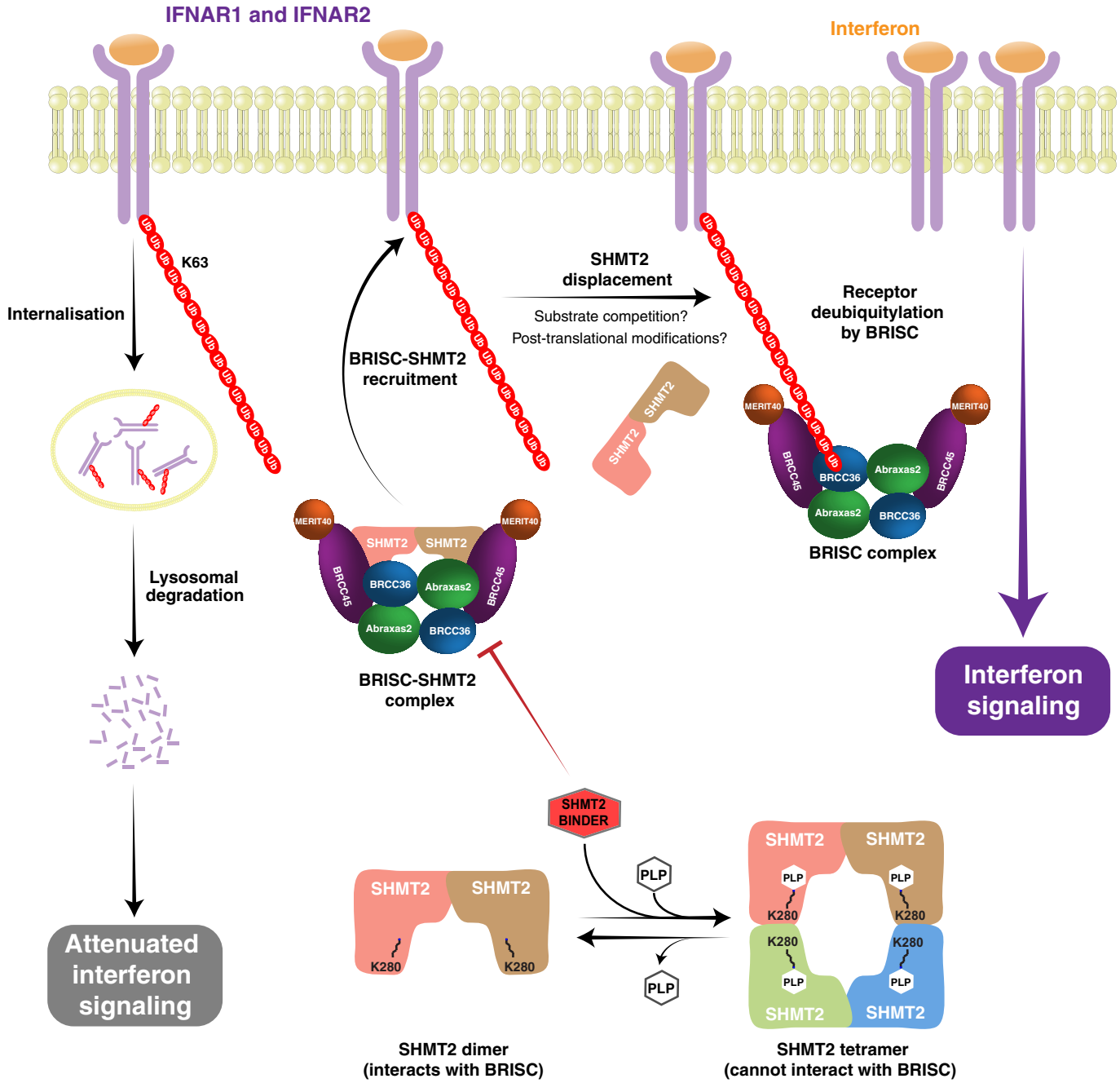

Extended Data Fig. 10 | Proposed model of BRISC–SHMT2 regulation of cytokine signalling. K63-linked poly-ubiquitylated interferon receptors (IFNAR1 and IFNAR2) are internalized and degraded through the lysosomal degradation pathway. The BRISC–SHMT2 complex is required for deubiquitylation of IFNAR1 and IFNAR2, and for receptor stabilization. BRISC deubiquitylation of IFNAR1 and IFNAR2 receptors proceeds after SHMT2 displacement, which leads to sustained interferon signalling. The SHMT2 dimer–tetramer transition is regulated by PLP binding. Only an inactive SHMT2 dimer can interact with BRISC, whereas the active SHMT2 tetramer will sterically clash with the BRCC36–Abraxas 2 superdimer. Modulation of SHMT2 dimer–tetramer transition by PLP analogues or other binders could represent ways to inhibit BRISC recruitment to IFNAR1 and IFNAR2, and to reduce interferon signalling.

Extended Data Table 1 | Summary of data collection, image processing, model building, refinement and validation statistics

	BRISCΔNΔC-SHMT2 EMD-4759/EMD-4760, PDB 6R8F		BRISCΔNΔC-SHMT2	BRISCΔNΔC
Staining	None		Uranyl acetate	Uranyl acetate
Data Collection				
Microscope	FEI Titian KRIOS		FEI Tecnai F20	FEI Tecnai F20
Voltage (keV)	300		120	120
Detector	FEI Falcon III		FEI Ceta CMOS	FEI Ceta CMOS
Magnification	x75,000		x29,000	x29,000
Defocus range (μm)	-1.6 to -3.1			
Pixel size (Å)	1.065		3.51	3.51
Electron dose ($e^-/Å^2$)	Dataset 1: 95 Dataset 2: 83 Dataset 3: 86		15	15
Electron dose per frame ($e^-/Å^2$)	1.2			
Exposure (sec)	2		1.5	1.5
No. of frames	Dataset 1: 79 Dataset 2: 70 Dataset 3: 71		1	1
No. of micrographs	7,494		222	218
Data Processing	**Complete dataset**	**2-arm dataset**		
Symmetry Point Group	C1	C2		
Final particle number	403,499	64,403		
Map resolution (Å)	3.8	4.2		
FSC threshold	0.143	0.143		
Map resolution range (Å)	3.5 – 10.0	3.9 – 11.5		
Refinement				
Initial models used (PDB code)	5CW3, 6DK3	5CW3, 6DK3		
Map sharpening B-factor ($Å^2$)	-202	-182		
Model Composition				
Non-hydrogen atoms	15,810	15,810		
Protein residues	2,164	2,164		
Zinc ions	2	2		
R.M.S.D from ideal geometry				
Bonds lengths (Å)	0.01	0.01		
Bond angles (°)	1.07	1.00		
Validation				
Molprobity score	1.72 (88th percentile)	1.80 (85th percentile)		
Clashscore	3.53 (97th percentile)	4.53 (95th percentile)		
Poor rotamers (%)	0.00	0.27		
Ramachandran plot statistics				
Favored (%)	89.08	89.32		
Allowed (%)	10.92	10.68		
Disallowed (%)	0.00	0.00		

Author Queries

Journal: **Nature**
Paper: **s41586-019-1232-1**
Title: **Metabolic control of BRISC–SHMT2 assembly regulates immune signalling**

AUTHOR:

The following queries have arisen during the editing of your manuscript. Please answer by making the requisite corrections directly in the e.proofing tool rather than marking them up on the PDF. This will ensure that your corrections are incorporated accurately and that your paper is published as quickly as possible.

Query Reference	Query
Q1	This proof has been produced on the basis of your corrections to the preproof. For this later stage of production we use an online 'eproof' tool, where you can make corrections directly to the text within the tool and also mark up corrections to the copyedited figures. Please check that the display items are as follows(ms no: 2018-06-08607C): Figs 0 (black & white); 4 (colour); Tables: None; Boxes: None; Extended Data display items: 10 Fig., 1 table; SI: yes. The eproof contains the main-text figures edited by us and (if present) the Extended Data items (unedited except for the legends) and the Supplementary Information (unedited). Please note that the eproof should be amended in only one browser window at any one time, otherwise changes will be overwritten. Please check the edits to all main-text figures (and tables, if any) very carefully, and ensure that any error bars in the figures are defined in the figure legends. Extended Data items may be revised only if there are errors in the original submissions. If you need to revise any Extended Data items please upload these files when you submit your corrections to this preproof .
Q2	final sentence of abstract slightly re-worded; is this re-wording OK?
Q3	Please check your article carefully, coordinate with any co-authors and enter all final edits clearly in the eproof, remembering to save frequently. Once corrections are submitted, we cannot routinely make further changes to the article.
Q4	Note that the eproof should be amended in only one browser window at any one time; otherwise changes will be overwritten.
Q5	Author surnames have been highlighted. Please check these carefully and adjust if the first name or surname is marked up incorrectly. Note that changes here will affect indexing of your article in public repositories such as PubMed. Also, carefully check the spelling and numbering of all author names and affiliations, and the corresponding email address(es).

RESEARCH ARTICLE

Author Queries

Journal: **Nature**
Paper: **s41586-019-1232-1**
Title: **Metabolic control of BRISC–SHMT2 assembly regulates immune signalling**

AUTHOR:

The following queries have arisen during the editing of your manuscript. Please answer by making the requisite corrections directly in the e.proofing tool rather than marking them up on the PDF. This will ensure that your corrections are incorporated accurately and that your paper is published as quickly as possible.

Query Reference	Query
Q6	Please note that after the paper has been formally accepted you can only provide amended Supplementary Information files for critical changes to the scientific content, not for style. You should clearly explain what changes have been made if you do resupply any such files.
Q7	I added definition for UTF to the legend of Fig. 3a, b; is it correct? Please amend if necessary
Q8	please define 'exp.' in Fig. 3d

nature research

Corresponding author(s): Elton Zeqiraj and Roger A. Greenberg

Reporting Summary

Nature Research wishes to improve the reproducibility of the work that we publish. This form provides structure for consistency and transparency in reporting. For further information on Nature Research policies, see Authors & Referees and the Editorial Policy Checklist.

Statistical parameters

When statistical analyses are reported, confirm that the following items are present in the relevant location (e.g. figure legend, table legend, main text, or Methods section).

n/a	Confirmed	
☐	☒	The exact sample size (*n*) for each experimental group/condition, given as a discrete number and unit of measurement
☐	☒	An indication of whether measurements were taken from distinct samples or whether the same sample was measured repeatedly
☐	☒	The statistical test(s) used AND whether they are one- or two-sided *Only common tests should be described solely by name; describe more complex techniques in the Methods section.*
☒	☐	A description of all covariates tested
☒	☐	A description of any assumptions or corrections, such as tests of normality and adjustment for multiple comparisons
☒	☐	A full description of the statistics including central tendency (e.g. means) or other basic estimates (e.g. regression coefficient) AND variation (e.g. standard deviation) or associated estimates of uncertainty (e.g. confidence intervals)
☒	☐	For null hypothesis testing, the test statistic (e.g. *F*, *t*, *r*) with confidence intervals, effect sizes, degrees of freedom and *P* value noted *Give P values as exact values whenever suitable.*
☒	☐	For Bayesian analysis, information on the choice of priors and Markov chain Monte Carlo settings
☒	☐	For hierarchical and complex designs, identification of the appropriate level for tests and full reporting of outcomes
☒	☐	Estimates of effect sizes (e.g. Cohen's *d*, Pearson's *r*), indicating how they were calculated
☐	☒	Clearly defined error bars *State explicitly what error bars represent (e.g. SD, SE, CI)*

Our web collection on statistics for biologists may be useful.

Software and code

Policy information about availability of computer code

Data collection	Cryo-EM data were collected using ThermoFisher (previously FEI) EPU software. Negative stained data were collected using ThermoFisher (previously FEI) TEM imaging and analysis (TIA).
Data analysis	- Cryo-EM data and structural models were analysed using: Chimera (1.11.2), COOT (0.8.6), Phenix (1.11.1_2575), Relion (3.0), CCP4 (7.0), ResMap (1.1.4), MotionCorr2, gCTF (0.5), Pymol (1.8.6.0). - Mass spectrometry data was analysed using the following software: MassLynx v4.1, UniDec v2.7.1, Xcalibur Qual Browser v4.0.27.19.

For manuscripts utilizing custom algorithms or software that are central to the research but not yet described in published literature, software must be made available to editors/reviewers upon request. We strongly encourage code deposition in a community repository (e.g. GitHub). See the Nature Research guidelines for submitting code & software for further information.

Data

Policy information about availability of data

All manuscripts must include a data availability statement. This statement should provide the following information, where applicable:

- Accession codes, unique identifiers, or web links for publicly available datasets
- A list of figures that have associated raw data
- A description of any restrictions on data availability

Coordinates were deposited in the Protein Data Bank under accession code: 6R8F Cryo-EM reconstructions of BRISC-SHMT2 in C1 and C2 were deposited in the EM Data Bank under accession codes: EMD-4759 and EMD-4760. All maps and model coordinates will be publicly available upon or soon after publication.

Field-specific reporting

Please select the best fit for your research. If you are not sure, read the appropriate sections before making your selection.

☒ Life sciences ☐ Behavioural & social sciences ☐ Ecological, evolutionary & environmental sciences

For a reference copy of the document with all sections, see nature.com/authors/policies/ReportingSummary-flat.pdf

Life sciences study design

All studies must disclose on these points even when the disclosure is negative.

Sample size	Cryo-EM datasets were collected for a total of approx. 6 days of instrument time. Sample size for cryo-EM analysis was arbitrary chosen and depended on sample and instrument availability.
Data exclusions	During cryo-EM data processing, "bad" particles (particles which failed at the 2D or 3D classifications stage) were omitted according to current scientific standards and in line with standard practice. Full details of classifications are provided in the manuscript.
Replication	All replication attempts were successful and in line with accepted scientific standards. Experiments which were only run once because limited samples were available, are clearly mentioned in the figure legends. Where required, cross validation was performed by rational mutagenesis, multiple model systems and appropriate use of controls and orthogonal assays.
Randomization	No randomization during allocation into experimental groups was applicable. Where required, cross validation was performed by rational mutagenesis, multiple model systems and appropriate use of controls and orthogonal assays.
Blinding	Structure determinations were performed without blinding. The sample identity was known to the investigators as this was required for appropriate interpretation of electron microscopy maps and model building.

Reporting for specific materials, systems and methods

Materials & experimental systems

n/a	Involved in the study
☐	☒ Unique biological materials
☐	☒ Antibodies
☐	☒ Eukaryotic cell lines
☒	☐ Palaeontology
☒	☐ Animals and other organisms
☒	☐ Human research participants

Methods

n/a	Involved in the study
☒	☐ ChIP-seq
☒	☐ Flow cytometry
☒	☐ MRI-based neuroimaging

Unique biological materials

Policy information about availability of materials

Obtaining unique materials	All unique materials will be made available upon reasonable requests.

Antibodies

Antibodies used

Rabbit polyclonal antibodies were generated by the Greenberg lab to the following recombinant proteins: MERIT40, Abraxas2, BRCC36 and BRCC45.

Commercially available antibodies:
1. HA epitope (HA.11 Covance).
2. SHMT2 (Cell Signaling).
3. Ub (P4D1) HRP, Monoclonal Antibody (Santa Cruz)
4. Ub VU1 antibody (Lifesensors)
5. IFNAR1 antibody (Bethyl laboratories)
6. Phospho-Stat1 (Tyr701) (58D6) Rabbit mAb #9167 (Cell Signalling)
7. Stat1 Antibody #9172 (Cell Signalling)

Validation

Polyclonal antibodies were validated in house using knockout cell lines to verify that no detectable signal was observed on western blot in knockout cell lines for the cognate antigen.

Validation date for commercially available antibodies can be found using the links below:
1. HA epitope (HA.11 Covance). https://www.biolegend.com/fr-fr/global-elements/pdf-popup/anti-ha-11-epitope-tag-antibody-11071?filename=Anti-HA11%20Epitope%20Tag%20Antibody.pdf&pdfgen=true

2. SHMT2 (Cell Signaling). https://www.cellsignal.com/products/primary-antibodies/shmt2-antibody/12762

3. Ub P4D1 (Santa Cruz). https://datasheets.scbt.com/sc-8017.pdf

4. Ub VU1 (Lifesensors). https://lifesensors.com/wp-content/uploads/2017/02/VU101_VU-1Antibody_datasheet_032113.pdf

5. IFNAR1 antibody (Bethyl laboratories): https://www.bethyl.com/product/A304-290A/IFNAR1+Antibody

6. pSTAT1 (pY701) (Cell Signalling): https://media.cellsignal.com/pdf/9167.pdf

7. STAT1 (Cell Signalling): https://media.cellsignal.com/pdf/9172.pdf

Eukaryotic cell lines

Policy information about cell lines

Cell line source(s)

Sf9 cells used for protein expression were obtained from Invitrogen (Thermofisher). Abraxas null Mouse Embryonic fibroblasts (MEFs) were generated as previously described (Zheng et al. Cell Reports2013). HEK293T cells were obtained from ATCC.

Authentication

No authentication of Sf9 cells or HEK293T cells was carried out. Abraxas2 null mouse embryonic fibroblasts were verified by western blot and PCR genotyping.

Mycoplasma contamination

No mycoplasma contamination was detected using a commercial mycoplasma detection kit.

Commonly misidentified lines
(See ICLAC register)

Commonly misidentified cell lines were not used.